



SPA: 3D SPATIAL-AWARENESS ENABLES EFFECTIVE EMBODIED REPRESENTATION

Anonymous authors

Paper under double-blind review

ABSTRACT

In this paper, we introduce SPA, a novel representation learning framework that emphasizes the importance of 3D spatial awareness in embodied AI. Our approach leverages differentiable neural rendering on multi-view images to endow a vanilla Vision Transformer (ViT) with intrinsic spatial understanding. We present the most comprehensive evaluation of embodied representation learning to date, covering 268 tasks across 8 simulators with diverse policies in both single-task and language-conditioned multi-task scenarios. The results are compelling: SPA consistently outperforms more than 10 state-of-the-art representation methods, including those specifically designed for embodied AI, vision-centric tasks, and multi-modal applications, while using less training data. Furthermore, we conduct a series of real-world experiments to confirm its effectiveness in practical scenarios. These results highlight the critical role of 3D spatial awareness for embodied representation learning. Our strongest model takes more than 6000 GPU hours to train and we are committed to open-sourcing all code and model weights to foster future research in embodied representation learning.

1 INTRODUCTION

Vision systems have made remarkable progress in understanding 2D images (He et al., 2020; Chen et al., 2020a; He et al., 2022; Feichtenhofer et al., 2022; Tong et al., 2022; Yang et al., 2023; Oquab et al., 2023; Radford et al., 2021; Fang et al., 2023b; Chen et al., 2024b). However, achieving true visual intelligence necessitates a comprehensive understanding of the 3D world. This is crucial for embodied AI, where agents must perceive, reason, and interact with complex 3D environments.

Existing visual representation learning methods for embodied AI (Nair et al., 2022; Radosavovic et al., 2023; Majumdar et al., 2023; Karamcheti et al., 2023; Shang et al., 2024; Yang et al., 2024b) largely rely on paradigms from 2D vision, predominantly employing contrastive-based or masked autoencoder (MAE)-based approaches. However, they often struggle to fully capture the spatial relationships and 3D structures inherent in the physical world. This limitation arises from their primary emphasis on 2D semantic understanding, which, though valuable, is still insufficient for the sophisticated spatial reasoning required in embodied AI tasks, where agents need to navigate environments, manipulate objects, and make decisions using their 3D spatial awareness.

In this paper, we introduce SPA, a general 3D spatial-aware representation learning framework for embodied AI. SPA leverages neural rendering (Mildenhall et al., 2021) as the pre-training pre-text task on multi-view images. Unlike explicit 3D representations like point clouds or meshes—which prior work (Wang et al., 2024b;a; Ze et al., 2024; Zhu et al., 2024) has shown to outperform pure 2D inputs in robot learning—multi-view images are easier to process and more readily available, making them ideal for large-scale training, such as from internet videos. Specifically, given a vanilla 2D image backbone, *e.g.* a Vision Transformer (ViT) (Dosovitskiy et al., 2021), we first extract multi-view feature maps from the input images. Using known camera poses, we then construct a feature volume from these feature maps and sample rays to apply differentiable neural rendering. This process generates multi-view RGB-D images and semantic maps for supervision without labels, enabling the pre-training of a 2D image backbone to enhance 3D spatial awareness.

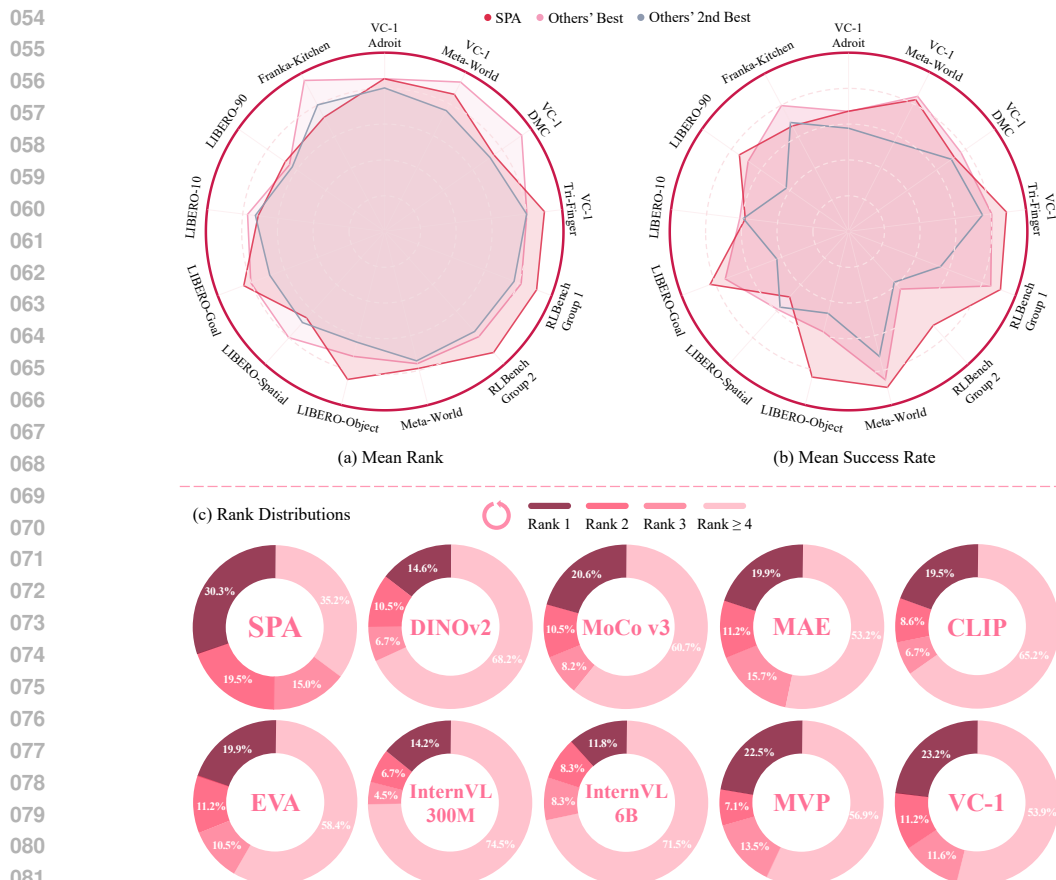


Figure 1: **Performance comparison across representations.** Above: (a) Mean rank and (b) mean success rate on benchmarks. Lines represent the performance of SPA, best, and second best performance on each benchmark. *Bottom*: Rank distributions for 268 individual tasks, showing proportions from rank 1 to rank ≥ 4 counterclockwise. Our model demonstrates superior overall performance.

To thoroughly validate our assumption and method, we collect 268 embodied tasks across 8 simulators using various policy methods. To our knowledge, this represents **the largest scale of embodied evaluation to date**. Previous work, such as R3M (Nair et al., 2022) and VC-1 (Majumdar et al., 2023), evaluated fewer than 20 tasks, potentially leading to incomplete or biased conclusions. Our evaluation spans both single-task and language-conditioned multi-task learning. We compare over 10 state-of-the-art representation learning methods, categorized as embodied-specific (Nair et al., 2022; Majumdar et al., 2023; Radosavovic et al., 2023), vision-centric (Oquab et al., 2023; Chen et al., 2021; He et al., 2022), and multi-modal (Radford et al., 2021; Fang et al., 2023b; Chen et al., 2024b). Our method consistently outperforms others, underscoring the importance of 3D spatial awareness for embodied AI. Notably, multi-modal models like CLIP (Radford et al., 2021), consistently perform poorly. This holds even the vision-language model scales the ViT to 6B parameters (Chen et al., 2024b). Through a camera pose estimation task and feature map visualization, we demonstrate that SPA has learned superior 3D spatial understanding. Further, we find that 3D awareness shows a positive correlation with embodied performance. Finally, we conduct several real-world tasks, where SPA also demonstrates superior performance. Our contribution can be summarized as follows.

- We propose a significant *spatial hypothesis*: 3D spatial awareness is crucial for embodied representation learning. Our experiments provide clear evidence for the hypothesis.
- We introduce SPA, a novel paradigm for representation learning in embodied AI. It enhances a vanilla Vision Transformer (ViT) with 3D awareness using differentiable neural rendering as the pre-text task on multi-view images.
- We conduct the largest evaluation benchmark for embodied representation learning, significantly larger than previous studies. It involves 268 tasks, 8 simulators, and over 10 SOTA methods with diverse downstream policies and task settings.

- Through extensive experiments in both simulators and real-world settings, SPA outperforms more than 10 SOTA representation learning methods, demonstrating its effectiveness.

2 METHODOLOGY

In this section, we first describe our process for handling multi-view image inputs and feature extraction in Sec. 2.1. Subsequently, we construct an explicit feature volume from these multi-view features, detailed in Sec. 2.2. Finally, we explain the image rendering from the feature volume and loss functions for network optimization in Sec. 2.3 and Sec. 2.4. Our pipeline is visualized in Fig. 2.

2.1 INPUT PROCESS AND FEATURE EXTRACTION

Given a set of multi-view images $\mathbf{I} = \{I_1, I_2, \dots, I_N\}$, where each $I_i \in \mathbb{R}^{3 \times H \times W}$ and $N \in \mathbb{Z}^+$, we utilize a 2D image backbone F , such as a ViT. The images are processed separately through F , yielding latent features $\mathbf{L} = \{l_1, l_2, \dots, l_N\}$, where each $l_i = F(I_i) \in \mathbb{R}^{L \times C}$. Following MAE, we apply random masking to input images to enhance robustness, but without a ViT decoder and MAE’s pixel reconstruction objective. For each l_i , masked positions are filled with a mask token, and we concatenate the global class token with other patch tokens as read-out tokens similar to DPT (Ranftl et al., 2020). We then unpatchify them to obtain a latent feature map of size $\frac{H}{P} \times \frac{W}{P}$, where P is the ViT patch size. Finally, two simple upsampling layers transform this into a feature map M_i matching the input resolution. Each upsampling layer includes a convolution, a GELU (Hendrycks & Gimpel, 2016) activation, and a pixel shuffle layer (Shi et al., 2016) with an upscale factor of \sqrt{P} .

2.2 DYNAMIC VOLUME CONSTRUCTION

To enable multi-view interaction, we construct a 3D feature volume from multi-view feature maps, \mathbf{M} . Unlike the bird’s-eye view (BEV) construction in autonomous driving (Li et al., 2022), which usually relies on a fixed scene range around ego vehicle, our method dynamically adjusts the scene range based on the spatial extents of the environment to accommodate varying datasets. Specifically, the scene’s bounds are first estimated using available depth data, sparse points, or pre-defined rules. We then partition the scene into a volume of size $X \times Y \times Z$, with voxel size dynamically adjusted to capture either fine object details or larger environments. Voxel features, $\tilde{\mathcal{V}}$, are initialized with learnable positional embeddings. Each voxel is projected onto the multi-view feature maps using the known transformation matrix \mathbf{T} . Deformable attention (Zhu et al., 2021) is then applied, where the multi-view features act as keys and values, and the voxel features as queries. Finally, a 3D convolution refines the output volume features to obtain \mathcal{V} . The process can be formulated as:

$$\mathcal{V} = \text{Conv3D}(\text{DeformAttn}(\tilde{\mathcal{V}}, \mathbf{M}, \mathbf{T})). \quad (1)$$

2.3 DIFFERENTIABLE VOLUMETRIC RENDERING

After constructing the feature volume, we employ differentiable neural rendering (Mildenhall et al., 2021) to connect 2D and 3D domains. For better geometry representation, we utilize the implicit signed distance function (SDF) field modeling as in NeuS (Wang et al., 2021). The SDF represents the 3D distance from a query point to the nearest surface, implicitly capturing the 3D geometry.

Given a feature volume \mathcal{V} , we apply a shallow 3D CNN ϕ to directly produce three outputs: an SDF feature volume $\mathcal{S} \in \mathbb{R}^{X \times Y \times Z}$, a spherical harmonic (SH) (Yu et al., 2021; Zhu et al., 2023a) coefficient field $\mathcal{K} \in \mathbb{R}^{D \times X \times Y \times Z}$ (where $D = 3 \cdot (l_{\max} + 1)^2$) for color rendering, and a semantic feature volume $\mathcal{F} \in \mathbb{R}^{C_{\text{semantic}} \times X \times Y \times Z}$:

$$\mathcal{S} \in \mathbb{R}^{X \times Y \times Z}, \quad \mathcal{K} \in \mathbb{R}^{D \times X \times Y \times Z}, \quad \mathcal{F} \in \mathbb{R}^{C_{\text{semantic}} \times X \times Y \times Z} = \phi(\mathcal{V}). \quad (2)$$

Unlike prior work (Huang et al., 2023; Zhu et al., 2023b; Yang et al., 2024a), which employs an MLP to compute the attributes of each sampled point individually, we directly apply a 3D CNN to \mathcal{V} . This eliminates the need for pointwise MLP computations, reducing redundant processing and enabling more efficient execution. Consequently, our approach leads to substantial improvements in both time and memory efficiency, especially when sampling a large number of points during rendering.

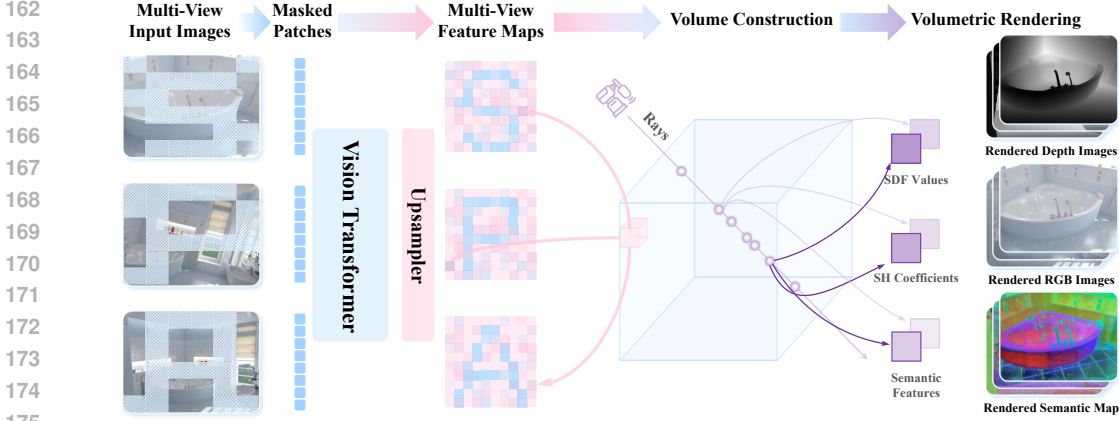


Figure 2: **Pipeline Overview.** Given multi-view images, we randomly mask patches and input the remaining into a Vision Transformer. The upsampled latent features generate multi-view feature maps, from which we construct a feature volume to derive SDF values, SH coefficients, and semantic features. We then render depth, RGB, and semantic maps for loss computation.

To render a 2D pixel i , we sample N ray points $\{\mathbf{p}_j = \mathbf{o} + t_j \mathbf{d}_i \mid j = 1, \dots, N, t_j < t_{j+1}\}$ from ray \mathbf{r}_i , where \mathbf{o} is the camera origin and \mathbf{d}_i is the viewing direction. Attributes for each point are obtained via trilinear sampling:

$$s_j = \tau(\mathcal{S}, \mathbf{p}_j), \quad \mathbf{k}_j = \tau(\mathcal{K}, \mathbf{p}_j), \quad \mathbf{f}_j = \tau(\mathcal{F}, \mathbf{p}_j). \quad (3)$$

The SH vector $\mathbf{k}_j = (k_l^m)_{0 \leq l \leq l_{\max}, -l \leq m \leq l}$, where $k_l^m \in \mathbb{R}^3$, is used to compute view-dependent colors $\hat{\mathbf{c}}_j$ by querying the SH basis functions $Y_l^m : \mathbb{S}^2 \rightarrow \mathbb{R}$ based on the viewing direction \mathbf{d}_j :

$$\hat{\mathbf{c}}_j = \text{Sigmoid} \left(\sum_{l=0}^{l_{\max}} \sum_{m=-l}^l k_l^m Y_l^m(\mathbf{d}_j) \right). \quad (4)$$

Following the formulation in NeuS (Wang et al., 2021), the RGB color $\hat{\mathbf{C}}_i$, depth $\hat{\mathbf{D}}_i$, and semantic feature $\hat{\mathbf{F}}_i$ for pixel i are computed by integrating the predicted values along the ray:

$$\hat{\mathbf{C}}_i = \sum_{j=1}^N w_j \hat{\mathbf{c}}_j, \quad \hat{\mathbf{D}}_i = \sum_{j=1}^N w_j t_j, \quad \hat{\mathbf{F}}_i = \sum_{j=1}^N w_j \hat{\mathbf{f}}_j, \quad (5)$$

where $w_j = T_j \alpha_j$ is the occlusion-aware weight, with $T_j = \prod_{k=1}^{j-1} (1 - \alpha_k)$ representing the accumulated transmittance and α_j being the opacity value. Specifically, α_j is computed as:

$$\alpha_j = \max \left(\frac{\sigma_s(s_j) - \sigma_s(s_{j+1})}{\sigma_s(s_j)}, 0 \right), \quad (6)$$

where $\sigma_s(x) = (1 + e^{-sx})^{-1}$ is the sigmoid function modulated by a learnable parameter s .

2.4 LOSS FUNCTIONS

During pre-training, we randomly sample K pixels from multi-view inputs in each iteration. The rendering loss is calculated based on the differences between the input pixel values and the predicted values. For the semantic feature map, we use the feature map from AM-RADIO (Ranzinger et al., 2024) as supervision. Our framework has the capability to distill knowledge from multiple vision foundation models by adding multiple rendering heads. However, this paper does not explore that approach, as it is not the primary focus. The rendering loss is expressed as:

$$\mathcal{L}_{\text{render}} = \frac{1}{K} \sum_{i=1}^K \left(\lambda_{\text{color}} \cdot \|\mathbf{C}_i - \hat{\mathbf{C}}_i\| + \lambda_{\text{depth}} \cdot \|\mathbf{D}_i - \hat{\mathbf{D}}_i\| + \lambda_{\text{semantic}} \cdot \|\mathbf{F}_i - \hat{\mathbf{F}}_i\| \right). \quad (7)$$

Additionally, we incorporate the Eikonal regularization loss $\mathcal{L}_{\text{eikonal}}$, near-surface SDF supervision loss \mathcal{L}_{sdf} , and free space SDF loss $\mathcal{L}_{\text{free}}$, which are standard in neural surface reconstruction. Detailed definitions of these losses are provided in Appendix A. The total loss is defined as:

$$\mathcal{L}_{\text{total}} = \mathcal{L}_{\text{render}} + \lambda_{\text{eikonal}} \cdot \mathcal{L}_{\text{eikonal}} + \lambda_{\text{sdf}} \cdot \mathcal{L}_{\text{sdf}} + \lambda_{\text{free}} \cdot \mathcal{L}_{\text{free}}. \quad (8)$$

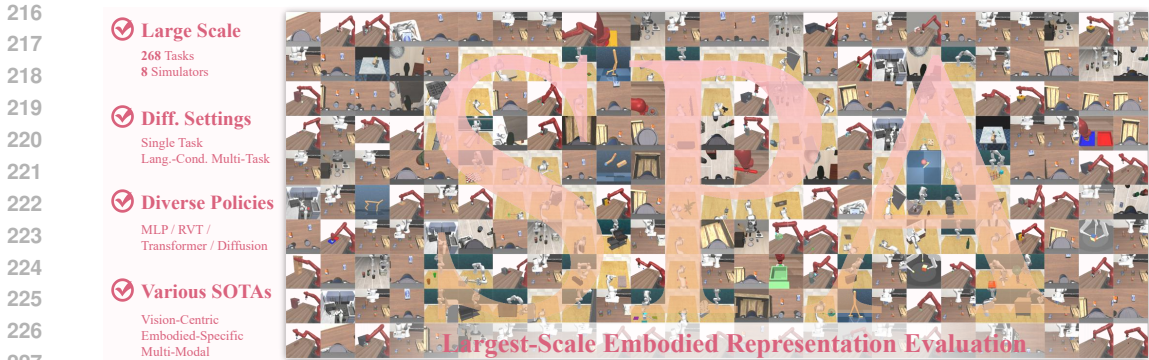


Figure 3: **Overview of our large-scale embodied evaluation.** We conduct the largest-scale evaluation of embodied representation learning to date. Our study encompasses 268 tasks across 8 simulators, including both single-task and language-conditioned multi-task settings. We evaluate diverse policy architectures and assess various state-of-the-art representation methods. This thorough evaluation allows us to provide a comprehensive and unbiased analysis of different representations.

3 LARGE-SCALE EMBODIED EVALUATION

Unlike the CV or NLP communities, where large-scale benchmarks are common, embodied representations have not been thoroughly assessed. The largest previous evaluation, VC-1 (Majumdar et al., 2023), includes only 17 tasks. This may lead to randomness and bias. Therefore, we have created **the largest embodied evaluation to date**, encompassing **268 tasks** across 8 simulators—**over 15 times larger** than VC-1’s evaluation. Additionally, unlike previous approaches (Majumdar et al., 2023; Nair et al., 2022; Radosavovic et al., 2023) that used a small MLP policy under single-task settings, our evaluation spans multiple policy types (*e.g.* MLP, diffusion, transformer) and includes both single-task and language-conditioned multi-task settings. This unprecedented scale and diversity ensure robust and convincing conclusions. During all evaluations, we adhere to standard practices by freezing the pre-trained representation model. Our detailed evaluation settings can be found in Appendix B. The overview of our evaluation is shown in Fig. 3.

We have included 3 *single-task benchmarks*:

- 1) **VC-1** (Majumdar et al., 2023) involves 4 selected simulators with 14 tasks in total: Adroit (AD) (Kumar, 2016), Meta-World (MW) (Yu et al., 2020), DMControl (DMC) (Tunyasuvunakool et al., 2020), and TriFinger (TF) (Wüthrich et al., 2020). We use a 3-layer MLP as the policy network.
- 2) **Franka Kitchen** (Gupta et al., 2019) involves 5 selected tasks. Each task spans two camera viewpoints and three random seeds. We utilize 25 demonstrations to train a 2-layer MLP policy.
- 3) **Meta-World** (Yu et al., 2020) involves 48 selected tasks of varying difficulty. We implemented the Diffusion Policy (Chi et al., 2023) on this benchmark and adhered to the setup in Ze et al. (2024) to generate 10 demonstrations for each single-task training, followed by evaluation through 20 rollouts.

We have also included 2 *language-conditioned multi-task benchmarks*:

- 1) **RLBench** (James et al., 2020) features 71 selected tasks that can be successfully executed. We divide the tasks into two groups according to their category defined by PolarNet (Chen et al., 2023). We employ RVT-2 (Goyal et al., 2024), the SOTA method on this benchmark, as our policy.
- 2) **LIBERO** (Liu et al., 2024) comprises 130 tasks across 5 suites: LIBERO-Spatial, LIBERO-Object, LIBERO-Goal, LIBERO-10, and LIBERO-90. We train a language-conditioned transformer policy provided by the original LIBERO on each suite with only 20 demonstrations per task.

4 TRAINING AND IMPLEMENTATION DETAILS

In this section, we present the implementation and training of our SPA model. We first compile several multi-view datasets, training ViT-B models on each to assess the impact of different datasets (Sec. 4.1). Finally, we integrate all factors and scale up both data and model size to train the strongest version of SPA using a ViT-large (ViT-L) backbone (Sec. 4.2). More details can be found in Appendix C.

4.1 DATASET INVESTIGATION

We collect several multi-view datasets. To investigate their effectiveness in SPA representation learning, we train a ViT-B model on one or two of the datasets, keeping the total training steps constant, and assess performance on the VC-1 benchmarks. For simplicity, semantic rendering is disabled. The datasets investigated are listed in the first column of Tab. 1. Most datasets provide ground-truth depth, which we use for supervision. As our findings above reveal that depth supervision is helpful, for datasets lacking ground-truth depth, we employ a depth estimation model. For instance, Droid (Khazatsky et al., 2024) only offers binocular images, so we apply CroCo-Stereo (Weinzaepfel et al., 2023) for dense depth estimation. Additionally, due to inaccurate camera poses in Droid, we treat its data as single-view inputs. The results are presented in Tab. 1, with further details in Appendix C. Our analysis reveals that some datasets can be detrimental. For example, although RH20T (Fang et al., 2023a) is a large-scale robotic dataset, its lack of visual diversity—stemming from data collected in the same lab—negatively impacts representation learning.

Table 1: **Influence of different datasets.** We present the performance results on the VC-1 benchmark. *Mean S.R.* refers to the mean success rate across all individual tasks.

Datasets	AD	MW	DMC	TF	Mean S.R.
ScanNet (Dai et al., 2017)	52.67±4.11	90.93±3.22	65.11±1.31	70.75±1.08	73.68
ScanNet++ (Yeshwanth et al., 2023)	56.00±2.83	89.87±4.20	62.24±4.51	71.28±0.38	72.51
Arkitscenes (Baruch et al., 2021)	50.67±5.73	89.87±4.59	60.51±2.55	66.54±0.13	70.45
Droid (Khazatsky et al., 2024)	53.33±5.25	90.40±4.90	60.99±3.72	73.28±0.61	72.16
Hypersim (Roberts et al., 2021)	52.67±4.11	88.80±3.27	60.84±2.06	72.29±0.47	71.29
Hypersim + ADT (Pan et al., 2023)	52.00±2.83	87.20±2.30	63.61±1.04	70.83±0.13	71.41
Hypersim + S3DIS (Armeni et al., 2017)	49.33±0.94	94.13±2.04	64.57±3.91	71.74±0.75	73.98
Hypersim + Structured3D (Zheng et al., 2020)	46.67±4.11	80.27±7.72	58.02± 2.34	65.05±0.40	65.35
Hypersim + RH20T (Fang et al., 2023a)	47.33±1.89	86.93±4.99	57.01±4.35	64.28±0.46	67.35
Hypersim + ASE (Avetisyan et al., 2024)	47.33±4.11	87.73±3.39	60.62±4.14	68.59±0.30	69.54

4.2 PUT ALL TOGETHER

Based on the previous analyses, we proceed to pre-train the final version of SPA. We use a mask ratio of 0.5 and enable all three rendering losses. Following Ponder (Huang et al., 2023), we set the weight for the RGB loss to 10, the weights for the depth and semantic losses to 1, and use $\lambda_{\text{eikonal}} = 0.01$, $\lambda_{\text{sdf}} = 10$, and $\lambda_{\text{free}} = 1$. The volume size is $128 \times 128 \times 32$. For stable training, we apply the Exponential Moving Average (EMA) technique with a decay of 0.999. We use AdamW (Loshchilov et al., 2017) as the optimizer with a weight decay of 0.04 and a learning rate of $8e^{-4}$. OneCycle (Smith & Topin, 2019) learning rate scheduler is adopted. We utilize 80 NVIDIA A100-SXM4-80GB GPUs, each with a batch size of 2, and accumulate gradients over 8 batches, resulting in a total effective batch size of $2 \times 8 \times 80 = 1280$. Training is conducted over 2000 epochs, sampling each dataset to match the size of ADT per epoch. The datasets used for the final version include ScanNet, ScanNet++, ADT, S3DIS, Hypersim, and Droid.

5 EXPERIMENT RESULTS

In this section, we present the results of our large-scale evaluation. Our experiments are designed to address the following research questions:

- Q1:** How does SPA compare to other methods in our large-scale embodied evaluation?
- Q2:** What insights do we gain about various representation learning approaches from our evaluation?
- Q3:** Does SPA really learn enhanced 3D awareness that results in improved embodied representation?
- Q4:** Can SPA facilitate robot learning in real-world environments in a zero-shot manner?

5.1 OVERALL COMPARISONS (Q1, Q2)

Evaluation Metrics. We follow prior work (Majumdar et al., 2023; Zhu et al., 2024) in reporting two metrics: *Mean Success Rate (Mean S.R.)* and *Mean Rank*. Mean S.R. is the average success rate across all tasks, indicating overall performance, while Mean Rank reflects the average ranking of each method’s success rate across tasks, providing a measure of relative performance. Since RL Bench has fixed train and test sets, we report a single result for this benchmark.

Table 2: **Summary of different representation learning methods.** ‘#Param.’ is the total parameters of the encoder, while ‘#Frames’ indicates the total number of image frames used during pre-training.

Method	Vision-Centric			Multi-Modal				Embodied-Specific			Distilled AM-RADIO (Ranzinger et al., 2024)
	MoCoV3 (Chen et al., 2020b)	MAE (He et al., 2023)	DINOv2 (Oquab et al., 2023)	CLIP (Radford et al., 2021)	EVA (Fang et al., 2023b)	InternViT-300M (Chen et al., 2023b)	InternViT-6B (Chen et al., 2024b)	MVP (Radosavovic et al., 2023)	VC-1 (Majumdar et al., 2023)	SPA (Ours)	
Is Vanilla?	✓	✓	✗	✓	✓	✗	✗	✓	✓	✓	✗
Input Size	224	224	224	224	224	448	224	256	224	224	224
Patch Size	16	16	14	14	14	14	14	16	16	16	16
#Param.	303M	303M	303M	303M	303M	303M	5.9B	303M	303M	303M	653M
#Frames	1.28M	1.28M	1.2B	400M	14M	5.0B	5.0B	4.5M	5.6M	3.8M	1.4B

Table 3: **Comparison of different representation learning methods.** ‘OOM’ indicates an out-of-memory error during evaluation. The best and second-best results are **bolded** and underlined respectively. The number in parentheses denotes the number of tasks. **S.R. denotes ‘Success Rate’.**

Method		Vision-Centric			Multi-Modal			Embodied-Specific			
Benchmark		MoCoV3	MAE	DINOv2	CLIP	EVA	InternViT-300M	InternViT-6B	MVP	VC-1	SPA (Ours)
VC-1	AD (2)	58.7±7.0	58.0±2.0	47.3±3.1	48.7±3.1	58.0±6.0	53.3±3.1	60.0±9.2	53.3±4.2	54.0±4.0	60.0±4.0
	MW (5)	88.8±5.0	90.0±4.6	84.0±3.7	77.1±3.2	90.7±0.9	84.0±3.7	89.1±1.2	93.6±5.2	87.5±3.8	93.3±2.0
	DMC (5)	67.3±3.3	74.4±1.8	64.5±2.5	53.9±3.6	62.7±2.8	53.3±0.4	66.3±3.2	69.4±2.6	65.3±3.6	<u>71.1±5.0</u>
	TF (2)	67.9±0.2	73.0±0.5	68.5±0.4	56.1±1.6	67.2±0.2	65.2±1.6	70.7±0.9	<u>73.2±0.8</u>	70.9±1.1	73.6±2.0
RLBench	Group 1 (35)	73.7	78.3	78.2	76.8	75.2	74.1	OOM	76.2	80.1	80.5
	Group 2 (36)	54.2	<u>57.7</u>	56.1	55.7	57.0	54.9	OOM	56.3	55.7	61.2
Meta-World (48)		69.3±1.5	67.8±1.7	56.3±0.6	66.7±1.7	63.7±1.3	57.5±1.7	OOM	66.4±1.7	68.6±1.5	69.2±1.7
LIBERO	Object (10)	65.3±8.0	71.7±13.1	64.7±9.9	50.2±7.0	73.2±6.0	67.7±6.0	58.0±10.6	63.7±4.8	69.7±7.2	76.7±5.3
	Spatial (10)	40.5±0.9	57.2±2.9	36.3±11.8	32.2±0.6	59.3±7.7	48.3±6.4	42.0±10.3	58.0±6.2	50.5±7.5	50.0±3.8
	Goal (10)	49.2±8.1	54.3±6.0	22.2±2.3	30.3±3.2	56.8±2.9	58.8±4.5	33.2±2.0	<u>63.8±2.8</u>	57.5±6.6	65.3±2.5
	10 (10)	34.2±3.8	41.2±4.5	28.3±3.0	27.5±3.9	43.3±2.8	38.2±1.3	34.3±4.6	39.0±0.9	39.7±3.5	40.2±3.6
	90 (90)	30.0±1.4	29.9±2.0	27.5±2.2	29.4±2.0	31.3±2.3	23.8±1.8	27.1±2.1	<u>32.1±3.5</u>	30.6±3.3	32.2±1.6
Franka-Kitchen (5)		48.3±4.7	<u>42.7±2.6</u>	40.9±6.4	30.8±3.3	37.3±1.3	28.5±1.7	OOM	34.3±6.1	37.5±3.5	40.6±1.9
Mean S.R. ↑		81.67	<u>85.13</u>	75.18	77.10	83.84	75.41	30.65	84.85	84.69	88.63
Mean Rank ↓		4.51	<u>4.07</u>	5.61	5.17	4.37	5.92	7.57	4.24	4.13	3.20

Baselines. We evaluate 9 SOTA representation learning models, all using ViT-L backbone, categorized into vision-centric, multi-modal, and embodied-specific. This also includes a 6B multi-modal model (Chen et al., 2024b). The vision-centric methods are originally from the vision community; the multi-modal methods are typically CLIP-style language-image pre-trained models and are used specifically for VLMs; the embodied-specific methods are designed and pre-trained specifically for embodied AI tasks. Details are summarized in Tab. 2. The results on each benchmark are shown in Tab. 3. For detailed results on each task and each random seed, please refer to Appendix D. We also have visualized the performance radar chart and the per-task rank distributions in Fig. 1.

Finding 1: We observe that SPA demonstrates superior performance in both mean success rate and mean rank. While no method ranks first across all individual benchmarks, consistent with the findings by Majumdar et al. (2023), SPA achieves the best or second-best mean success rate in **11 out of 13 benchmarks**. Additionally, it ranks in the top 3 for **over 65.5% of individual tasks**, surpassing the second and third highest percentages of 46.8% for MAE and 46.0% for VC-1, respectively. These trends demonstrate the robustness and superiority of SPA.

Finding 2: We observe that for vision-centric methods, superior performance on vision tasks does **not** necessarily translate to better embodied performance. Despite using 10 times more data, DINOv2 performs worse than MoCoV3 and MAE. Notably, MAE performs exceptionally well, likely due to its reconstruction objective, which enhances *2D spatial awareness*. Interestingly, methods like MVP and VC-1, which are MAE models pre-trained on human interaction data, show **no clear advantage** over ImageNet (Deng et al., 2009) pre-trained MAE. This suggests that while human activity data may seem more relevant, data diversity and thorough convergence are more critical.

Finding 3: Multimodal methods **generally perform poorly** in embodied evaluations, except EVA, which combines image-language contrastive techniques with MAE reconstruction. Furthermore, InternViT-6B, despite having significantly more model parameters, does not demonstrate superiority and even performs worse on some benchmarks compared to InternViT-300M. This indicates that current scaling properties of multimodal approaches do not effectively translate to embodied AI.

Finding 4: Focusing on a single benchmark can **lead to highly biased conclusions**. For instance, ImageNet pre-trained methods (e.g. MoCoV3 and MAE) perform exceptionally well on the Franka Kitchen benchmark, suggesting a minimal domain gap between ImageNet and Franka Kitchen observations. Moreover, despite being based on MAE, previous SOTA embodied representations like MVP and VC-1 do not consistently outperform the original ImageNet version. These observations underscore the importance of our large-scale embodied evaluation.

Table 4: **Additional comparisons of ViT-base models.** S.R. denotes ‘Success Rate’.

Methods	DINOv2-B (Oquab et al., 2023)	MAE-B (He et al., 2022)	R3M-B (Nair et al., 2022)	VC-1-B (Majumdar et al., 2023)	STP-B (Yang et al., 2024b)	Voltron-B (Karamcheti et al., 2023)	Theia-B (Shang et al., 2024)	SPA-B (Ours)
Is Vanilla? Embodied?	✗ ✗	✓ ✗	✓ ✓	✓ ✓	✓ ✓	✗ ✓	✓ ✓	✓ ✓
VC-1	AD 60.80±0.80 MW 35.19±4.87 DMC 54.50±1.16 TF	52.67±3.06 88.80±4.00 62.39±4.97 70.78±0.17	48.00±6.93 59.20±5.60 49.57±4.85 56.18±7.00	50.00±5.29 86.67±0.92 60.92±0.70 72.33±0.69	52.00±2.00 92.00±1.39 61.40±2.86 67.96±0.95	46.67±4.62 84.00±3.20 56.36±2.01 74.26±1.57	53.33±5.03 89.07±3.23 64.98±3.42 69.41±0.60	52.00±3.46 92.00±4.16 64.21±3.52 73.06±0.51
Mean S.R.	47.31	71.63	54.37	70.19	71.92	69.50	<u>72.55</u>	73.66

Table 5: **Zero-shot camera pose estimation.** Trans. and Rot. denote ‘translation’ and ‘rotation’ errors respectively. The detailed metrics on the error calculation are listed in Appendix E.

Error	MoCoV3	MAE	DINOv2	CLIP	EVA	InternViT-300M	InternViT-6B	MVP	VC-1	SPA(Ours)
Trans. ($\times e^{-2}$)	2.29±0.07	2.15±0.07	6.55±0.07	4.21±0.37	5.49±0.24	4.62±0.14	5.39±0.41	2.15±0.12	2.02±0.07	1.65±0.09
Rot. ($\times e^{-1}$)	0.79±0.07	0.73±0.03	2.12±0.25	1.52±0.08	1.83±0.09	1.83±0.08	1.91±0.12	0.77±0.05	0.72±0.01	0.61±0.01

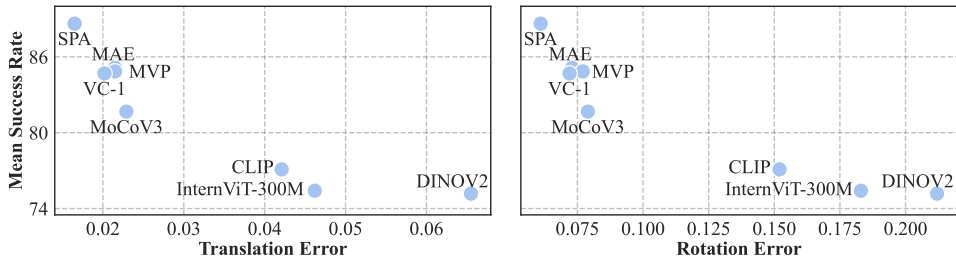


Figure 4: **Correlation between mean success rate and camera pose regression error.**

5.2 ADDITIONAL COMPARISONS (Q1)

We primarily compare with SOTA methods using the ViT-L backbone, which is commonly available and pre-trained on large-scale datasets. However, some embodied-specific models are only offered in ViT-B variants. Therefore, we provide additional comparisons with several ViT-B models in Tab. 4. Our ViT-B version, SPA-B, also outperforms other baselines. Furthermore, when compared to SPA-L on VC-1 benchmarks, the mean success rate increases by 4.16 (73.66 \rightarrow 77.82). This indicates that increasing the model size positively impacts SPA’s performance.

5.3 STUDY ON 3D AWARENESS OF SPA (Q3)

Firstly, we aim to provide clear evidence that the performance improvements of SPA are due to its 3D awareness. To demonstrate this, we conducted two additional ablation studies on the VC-1 benchmarks: 1) To determine whether the performance gain is due to SPA’s pre-training objectives or the datasets used, we continue pre-training the ImageNet pre-trained MAE-B (the most competitive method besides SPA) on the same datasets used by SPA-B, referring to this model as SPA-MAE. Hyperparameters, including mask ratio and batch size, are kept at their default settings, and both the ImageNet pre-trained encoder and decoder weights are initially loaded. 2) Since SPA uses the feature map of RADIO for semantic rendering supervision, we also evaluate the original RADIO (653M parameters) and its efficient version, E-RADIO (391M parameters). Results are presented in Tab. 6.

Table 6: Additional ablations on VC-1.

Methods	SPA-B	SPA-MAE	RADIO	E-RADIO
VC-1	AD 92.00±4.16 MW 64.21±3.52 DMC 73.06±0.51 TF	55.33±3.06 90.67±6.00 63.85±3.60 70.14±0.98	55.33±3.06 72.00±9.23 67.38±7.35 71.75±0.14	56.67±2.31 83.47±4.11 62.92±4.24 68.44±1.19
Mean S. R.	73.66	73.11	67.93	70.16

Finding 5: The 3D-aware pre-training objective significantly enhances SPA’s performance. It surpasses the single-image naive MAE with the same data. Notably, SPA learns superior representations compared to its semantic rendering teacher by a substantial margin.

Moreover, we provide both quantitative and qualitative evidence to demonstrate that SPA has acquired 3D awareness. For qualitative analysis, we visualize the zero-shot feature maps on multiview images of different encoder outputs, as shown in Fig. 5. The images are taken from the unseen Arkitscenes dataset. For quantitative analysis, we evaluate the zero-shot 3D awareness of various methods using a camera pose estimation task on the NAVI dataset (Jampani et al., 2023).

Specifically, given a pair of images from different viewpoints, we use a frozen encoder to extract features and concatenate them. A small MLP then regresses the relative camera pose and we report rotation and translation errors in Tab. 5. Details are in Appendix E. While El Banani et al. (2024) has explored 3D awareness of different vision models, their context differs. Their tasks can allow strong semantic models like DINOv2 to ‘cheat’. For example, multiview correspondence can be achieved through semantic matching, and the relative depth estimation task involves transforming normalized values into discrete bins, resembling a per-pixel classification task. Additionally, they emphasize fine-grained dense local context, whereas, embodied AI focuses more on sparse, global information (Nair et al., 2022). Thus, we believe camera pose estimation, which predicts a global ‘pose’ from observations, is more relevant to embodied AI, where a policy must predict a global ‘action’.

Finding 6: We observe that SPA outperforms all other methods in zero-shot camera pose estimation. It achieved an **18.3% improvement in translation and a 15.3% reduction in rotation error** compared to the second-best model. Additionally, we identify a **clear positive correlation** between camera pose estimation and embodied evaluation performance, as demonstrated in Fig. 4. This finding supports our spatial hypothesis and may offer valuable insights for future research on embodied representation.

Finding 7: The feature map visualization provides clear evidence that SPA has learned multi-view consistent knowledge, demonstrating its 3D awareness. Additionally, the features produced by SPA are **cleaner and more coherent**. Though VC-1 also generates smooth features, they are *not consistent across viewpoints*. The feature maps from the multi-modal approach are highly noisy and lack details.

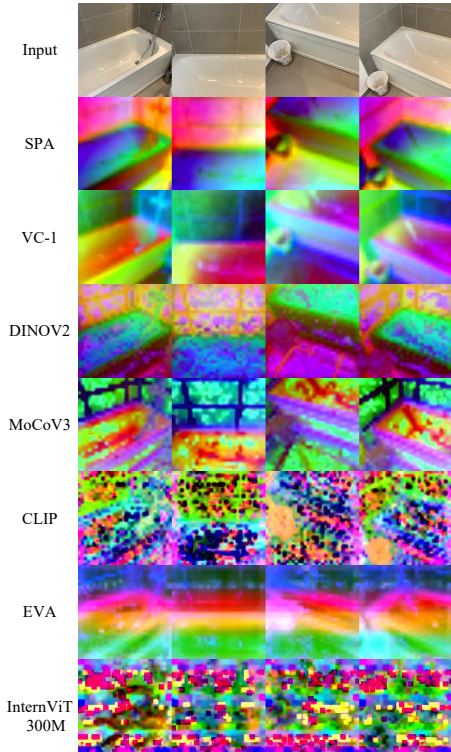


Figure 5: Feature map visualization.

5.4 HYPERPARAMETER INVESTIGATION

We conduct hyperparameter tuning with a ViT-B model on ScanNet (Dai et al., 2017), and evaluate it on VC-1 benchmarks, as shown in Tab. 7. **1) Mask Ratio.** Our results indicate that a mask ratio of 0.5 is the most effective. **2) Loss Components.** As discussed in Sec. 2.4, our rendering loss consists of color, depth, and semantic components. We sequentially deactivate each and find that all three are valuable. However, deactivating the semantic loss has the least impact.

Table 7: Mask ratio and loss components. C., D., S. denote color, depth, and semantic.

Mask Ratio	Loss			VC-1 Benchmark				Mean S.R.
	C.	D.	S.	AD	MW	DMC	TF	
0.00	✓	✓	✓	53.3±4.6	88.5±5.7	57.5±2.6	74.1±0.6	70.36
0.25	✓	✓	✓	52.7±3.1	89.6±4.5	57.6±3.0	70.4±1.7	70.17
0.50	✓	✓	✓	53.3±4.2	88.8±1.6	60.1±3.1	72.6±0.7	71.18
0.75	✓	✓	✓	51.3±1.2	88.0±3.5	61.1±3.5	73.0±0.8	71.01
0.95	✓	✓	✓	51.3±1.2	85.6±4.0	62.5±5.3	73.1±0.2	70.67
0.50	✓	✗	✓	51.3±1.2	90.9±3.3	58.8±5.6	71.5±1.0	71.01
0.50	✗	✓	✓	52.0±2.0	89.3±3.3	53.9±4.3	70.9±1.3	68.71
0.50	✓	✓	✗	52.7±3.1	88.0±4.5	61.5±3.4	71.6±1.2	71.16

5.5 REAL-WORLD EXPERIMENTS (Q4)

We conduct several real-world experiments to further investigate the generalization ability of different representations. Specifically, we utilize the open-sourced Low-Cost Robot Arm (Koch, 2024) to learn real-world tasks from pixels, with only 50 demonstrations per task using different frozen pre-trained representations. The robot performed two single-arm tasks: (1) picking a cube, and (2) stacking a yellow cube on a pink cube, as well as one dual-arm task: folding a cloth in half. Refer to Fig. 6 for illustrations and Appendix F for more details. We evaluate each task with 25 rollouts, with the results presented in Tab. 8. SPA consistently performs better on real-world tasks, suggesting that SPA’s pre-trained representations can robustly adapt to real-world environments without finetuning.

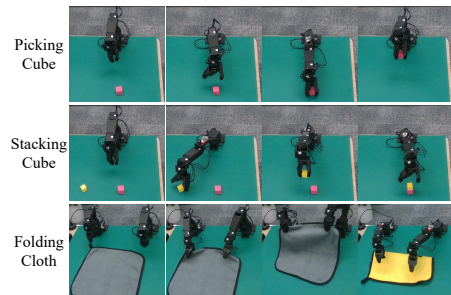


Figure 6: Real-world task illustrations.

Table 8: **Real-world experiment results. S.R. denotes ‘Success Rate’.**

Methods	MoCoV3	MAE	DINOv2	CLIP	EVA	InternViT-300M	InternViT-6B	MVP	VC-1	SPA (Ours)
Picking Cube	28.00	64.00	20.00	28.00	56.00	32.00	52.00	36.00	40.00	64.00
Stacking Cube	16.00	32.00	4.00	16.00	8.00	8.00	36.00	20.00	16.00	48.00
Folding Cloth	48.00	64.00	32.00	24.00	28.00	48.00	44.00	64.00	60.00	84.00
Mean S.R.	30.67	53.33	18.67	22.67	30.67	29.33	44.00	40.00	38.67	65.33

6 RELATED WORK

Representation Learning for Computer Vision. Recent advances in computer vision have increasingly focused on unsupervised and self-supervised learning to utilize large amounts of unlabeled data. Techniques like contrastive learning (Chen et al., 2020a; 2021; 2020b; He et al., 2020), masked autoencoders (He et al., 2022; Feichtenhofer et al., 2022; Bachmann et al., 2022; Tong et al., 2022; Wang et al., 2023), and self-distillation (Caron et al., 2021; Oquab et al., 2023; Ranzinger et al., 2024) have shown that effective representations can be learned without supervision. Moreover, multi-modal pre-training approaches (Radford et al., 2021; Fang et al., 2023b; Chen et al., 2024b) leverage language to learn more comprehensive representations. These developments have significantly improved transfer learning capabilities while also displaying zero-shot abilities.

Representation Learning for Embodied AI. Recent advances in embodied AI representation learning, inspired by computer vision, have applied techniques such as contrastive (Nair et al., 2022; Yang et al., 2023) and masked autoencoders (Radosavovic et al., 2023; Majumdar et al., 2023; Karamcheti et al., 2023; Yang et al., 2024b) to embodied AI. However, these approaches often emphasize semantic learning while overlooking the specific needs of embodied AI tasks. In this work, we propose a spatial hypothesis specifically for embodied AI representation learning, and we demonstrate how a standard 2D backbone can integrate 3D spatial awareness.

3D Robot Learning and 3D-Aware Computer Vision. Prior work in 3D robot learning has often relied on explicit 3D input (Zhu et al., 2024; Ze et al., 2024; Wang et al., 2024b;a; Shridhar et al., 2023; Chen et al., 2023), or lifting 2D features into 3D spaces (Ke et al., 2024; Goyal et al., 2024), providing a strong foundation for our spatial hypothesis. Given the scalability challenges of explicit 3D observations, some computer vision research has explored integrating 3D spatial awareness into 2D backbones (Yang et al., 2024a; Zhu et al., 2023b; Yue et al., 2025; Zhang et al., 2024). To the best of our knowledge, SPA is the first to systematically investigate this approach in embodied AI.

Neural Rendering. Recent advances in 3D vision, particularly in neural rendering (Mildenhall et al., 2021), have enabled the encoding of scenes using neural networks, which support differentiable rendering and reconstruction. Alongside improvements in neural rendering techniques themselves (Wang et al., 2021; Zhu et al., 2023a; Gropp et al., 2020; Ortiz et al., 2022; Wang et al., 2022), the Ponder series (Huang et al., 2023; Zhu et al., 2023b; Yang et al., 2024a) and subsequent works (Wang et al., 2024c; Irshad et al., 2024) have applied differentiable neural rendering for representation learning. However, they have primarily focused on 3D perception and autonomous driving scenarios. To the best of our knowledge, our work is the first to apply neural rendering for embodied AI representation learning using a standard 2D backbone, marking a novel contribution to this area of research.

7 CONCLUSION, LIMITATIONS, AND FUTURE WORK

In this work, we propose that 3D spatial awareness is crucial for embodied AI and introduce SPA, a novel framework that pre-trains a standard ViT backbone with 3D spatial awareness. To validate our hypothesis, we conduct the largest-scale embodied evaluation to date, over 15 times larger than previous studies. Our experiments demonstrate the clear superiority of SPA and highlight the importance of 3D awareness. Despite strong results across simulated and real robotic tasks, limitations remain. Our evaluation is currently restricted to imitation learning (specifically behavior cloning), and exploring SPA’s performance in other settings, such as reinforcement learning, presents an exciting future direction. **Incorporating SPA into VLMs to enhance their performance on spatial aware tasks (Chen et al., 2024a; Majumdar et al., 2024) also represents an exciting research area.** Additionally, SPA currently focuses on static multi-view scenes; extending it to dynamic, temporal scenarios could enhance its generality. Lastly, while we use the ViT encoder for fair comparison, the volume decoder’s multi-view interaction knowledge could be leveraged in policy learning, offering further potential for improvement.

REFERENCES

- 540
541
542 Iro Armeni, Sasha Sax, Amir R Zamir, and Silvio Savarese. Joint 2d-3d-semantic data for indoor
543 scene understanding. *arXiv preprint arXiv:1702.01105*, 2017.
544
- 545 Armen Avetisyan, Christopher Xie, Henry Howard-Jenkins, Tsun-Yi Yang, Samir Aroudj, Suvam
546 Patra, Fuyang Zhang, Duncan Frost, Luke Holland, Campbell Orme, et al. Scenescrypt: Reconstruct-
547 ing scenes with an autoregressive structured language model. *arXiv preprint arXiv:2403.13064*,
548 2024.
- 549 Roman Bachmann, David Mizrahi, Andrei Atanoy, and Amir Zamir. Multimaes: Multi-modal multi-
550 task masked autoencoders. In *European Conference on Computer Vision*, pp. 348–367. Springer,
551 2022.
552
- 553 Gilad Baruch, Zhuoyuan Chen, Afshin Dehghan, Tal Dimry, Yuri Feigin, Peter Fu, Thomas Gebauer,
554 Brandon Joffe, Daniel Kurz, Arik Schwartz, et al. Arkitscenes: A diverse real-world dataset for 3d
555 indoor scene understanding using mobile rgb-d data. *arXiv preprint arXiv:2111.08897*, 2021.
556
- 557 Mathilde Caron, Hugo Touvron, Ishan Misra, Hervé Jégou, Julien Mairal, Piotr Bojanowski, and
558 Armand Joulin. Emerging properties in self-supervised vision transformers. In *Proceedings of the*
559 *IEEE/CVF international conference on computer vision*, pp. 9650–9660, 2021.
- 560 Boyuan Chen, Zhuo Xu, Sean Kirmani, Brain Ichter, Dorsa Sadigh, Leonidas Guibas, and Fei Xia.
561 Spatialvlm: Endowing vision-language models with spatial reasoning capabilities. In *Proceedings*
562 *of the IEEE/CVF Conference on Computer Vision and Pattern Recognition*, pp. 14455–14465,
563 2024a.
564
- 565 Shizhe Chen, Ricardo Garcia, Cordelia Schmid, and Ivan Laptev. Polarnet: 3d point clouds for
566 language-guided robotic manipulation. 2023.
- 567 Ting Chen, Simon Kornblith, Mohammad Norouzi, and Geoffrey Hinton. A simple framework for
568 contrastive learning of visual representations. In *International conference on machine learning*, pp.
569 1597–1607. PMLR, 2020a.
570
- 571 Xinlei Chen, Haoqi Fan, Ross Girshick, and Kaiming He. Improved baselines with momentum
572 contrastive learning. *arXiv preprint arXiv:2003.04297*, 2020b.
573
- 574 Xinlei Chen, Saining Xie, and Kaiming He. An empirical study of training self-supervised vision
575 transformers. In *Proceedings of the IEEE/CVF international conference on computer vision*, pp.
576 9640–9649, 2021.
- 577 Zhe Chen, Jiannan Wu, Wenhai Wang, Weijie Su, Guo Chen, Sen Xing, Muyan Zhong, Qinglong
578 Zhang, Xizhou Zhu, Lewei Lu, et al. Internvl: Scaling up vision foundation models and aligning
579 for generic visual-linguistic tasks. In *Proceedings of the IEEE/CVF Conference on Computer*
580 *Vision and Pattern Recognition*, pp. 24185–24198, 2024b.
581
- 582 Cheng Chi, Siyuan Feng, Yilun Du, Zhenjia Xu, Eric Cousineau, Benjamin Burchfiel, and Shu-
583 ran Song. Diffusion policy: Visuomotor policy learning via action diffusion. *arXiv preprint*
584 *arXiv:2303.04137*, 2023.
- 585 RealRobot Contributors. Realrobot: A project for open-sourced robot learning research. <https://github.com/HaoyiZhu/RealRobot>. 2024.
586
587
- 588 Angela Dai, Angel X Chang, Manolis Savva, Maciej Halber, Thomas Funkhouser, and Matthias
589 Nießner. Scannet: Richly-annotated 3d reconstructions of indoor scenes. In *Proceedings of the*
590 *IEEE conference on computer vision and pattern recognition*, pp. 5828–5839, 2017.
591
- 592 Jia Deng, Wei Dong, Richard Socher, Li-Jia Li, Kai Li, and Li Fei-Fei. Imagenet: A large-scale
593 hierarchical image database. In *2009 IEEE conference on computer vision and pattern recognition*,
pp. 248–255. Ieee, 2009.

- 594 Alexey Dosovitskiy, Lucas Beyer, Alexander Kolesnikov, Dirk Weissenborn, Xiaohua Zhai, Thomas
595 Unterthiner, Mostafa Dehghani, Matthias Minderer, Georg Heigold, Sylvain Gelly, Jakob Uszkoreit,
596 and Neil Houlsby. An image is worth 16x16 words: Transformers for image recognition at scale.
597 *ICLR*, 2021.
- 598 Mohamed El Banani, Amit Raj, Kevis-Kokitsi Maninis, Abhishek Kar, Yuanzhen Li, Michael
599 Rubinstein, Deqing Sun, Leonidas Guibas, Justin Johnson, and Varun Jampani. Probing the 3d
600 awareness of visual foundation models. In *Proceedings of the IEEE/CVF Conference on Computer
601 Vision and Pattern Recognition*, pp. 21795–21806, 2024.
- 602 Hao-Shu Fang, Chenxi Wang, Minghao Gou, and Cewu Lu. Graspnet-1billion: A large-scale
603 benchmark for general object grasping. In *Proceedings of the IEEE/CVF conference on computer
604 vision and pattern recognition*, pp. 11444–11453, 2020.
- 605 Hao-Shu Fang, Hongjie Fang, Zhenyu Tang, Jirong Liu, Junbo Wang, Haoyi Zhu, and Cewu Lu.
606 Rh20t: A robotic dataset for learning diverse skills in one-shot. In *RSS 2023 Workshop on Learning
607 for Task and Motion Planning*, 2023a.
- 608 Yuxin Fang, Wen Wang, Binhui Xie, Quan Sun, Ledell Wu, Xinggang Wang, Tiejun Huang, Xinlong
609 Wang, and Yue Cao. Eva: Exploring the limits of masked visual representation learning at scale.
610 In *Proceedings of the IEEE/CVF Conference on Computer Vision and Pattern Recognition*, pp.
611 19358–19369, 2023b.
- 612 Christoph Feichtenhofer, Yanghao Li, Kaiming He, et al. Masked autoencoders as spatiotemporal
613 learners. *Advances in neural information processing systems*, 35:35946–35958, 2022.
- 614 Minghao Gou, Hao-Shu Fang, Zhanda Zhu, Sheng Xu, Chenxi Wang, and Cewu Lu. Rgb matters:
615 Learning 7-dof grasp poses on monocular rgbd images. In *2021 IEEE International Conference on
616 Robotics and Automation (ICRA)*, pp. 13459–13466. IEEE, 2021.
- 617 Ankit Goyal, Valts Blukis, Jie Xu, Yijie Guo, Yu-Wei Chao, and Dieter Fox. Rvt2: Learning precise
618 manipulation from few demonstrations. *RSS*, 2024.
- 619 Amos Gropp, Lior Yariv, Niv Haim, Matan Atzmon, and Yaron Lipman. Implicit geometric regular-
620 ization for learning shapes. *arXiv preprint arXiv:2002.10099*, 2020.
- 621 Abhishek Gupta, Vikash Kumar, Corey Lynch, Sergey Levine, and Karol Hausman. Relay policy
622 learning: Solving long-horizon tasks via imitation and reinforcement learning. *arXiv preprint
623 arXiv:1910.11956*, 2019.
- 624 Kaiming He, Haoqi Fan, Yuxin Wu, Saining Xie, and Ross Girshick. Momentum contrast for
625 unsupervised visual representation learning. In *Proceedings of the IEEE/CVF conference on
626 computer vision and pattern recognition*, pp. 9729–9738, 2020.
- 627 Kaiming He, Xinlei Chen, Saining Xie, Yanghao Li, Piotr Dollár, and Ross Girshick. Masked
628 autoencoders are scalable vision learners. In *Proceedings of the IEEE/CVF conference on computer
629 vision and pattern recognition*, pp. 16000–16009, 2022.
- 630 Dan Hendrycks and Kevin Gimpel. Gaussian error linear units (gelus). *arXiv preprint
631 arXiv:1606.08415*, 2016.
- 632 Yingdong Hu, Renhao Wang, Li Erran Li, and Yang Gao. For pre-trained vision models in motor
633 control, not all policy learning methods are created equal. In *International Conference on Machine
634 Learning*, pp. 13628–13651. PMLR, 2023.
- 635 Di Huang, Sida Peng, Tong He, Honghui Yang, Xiaowei Zhou, and Wanli Ouyang. Ponder: Point
636 cloud pre-training via neural rendering. In *Proceedings of the IEEE/CVF International Conference
637 on Computer Vision*, pp. 16089–16098, 2023.
- 638 Muhammad Zubair Irshad, Sergey Zakharov, Vitor Guizilini, Adrien Gaidon, Zsolt Kira, and Rares
639 Ambrus. Nerf-mae: Masked autoencoders for self-supervised 3d representation learning for neural
640 radiance fields. In *European Conference on Computer Vision (ECCV)*, 2024.

- 648 Stephen James, Zicong Ma, David Rovick Arrojo, and Andrew J Davison. Rlbench: The robot
649 learning benchmark & learning environment. *IEEE Robotics and Automation Letters*, 5(2):3019–
650 3026, 2020.
- 651
652 Varun Jampani, Kevis-Kokitsi Maninis, Andreas Engelhardt, Arjun Karpur, Karen Truong, Kyle
653 Sargent, Stefan Popov, André Araujo, Ricardo Martin Brualla, Kaushal Patel, et al. Navi: Category-
654 agnostic image collections with high-quality 3d shape and pose annotations. *Advances in Neural
655 Information Processing Systems*, 36:76061–76084, 2023.
- 656 Siddharth Karamcheti, Suraj Nair, Annie S. Chen, Thomas Kollar, Chelsea Finn, Dorsa Sadigh, and
657 Percy Liang. Language-driven representation learning for robotics. In *Robotics: Science and
658 Systems (RSS)*, 2023.
- 659
660 Tsung-Wei Ke, Nikolaos Gkanatsios, and Katerina Fragkiadaki. 3d diffuser actor: Policy diffusion
661 with 3d scene representations. *arXiv preprint arXiv:2402.10885*, 2024.
- 662
663 Alexander Khazatsky, Karl Pertsch, Suraj Nair, Ashwin Balakrishna, Sudeep Dasari, Siddharth
664 Karamcheti, Soroush Nasiriany, Mohan Kumar Srirama, Lawrence Yunliang Chen, Kirsty Ellis,
665 et al. Droid: A large-scale in-the-wild robot manipulation dataset. *arXiv preprint arXiv:2403.12945*,
2024.
- 666
667 Alexander Koch. Low-cost robot arm. [https://github.com/AlexanderKoch-Koch/
668 low_cost_robot](https://github.com/AlexanderKoch-Koch/low_cost_robot), 2024. URL [https://github.com/AlexanderKoch-Koch/low_
669 cost_robot](https://github.com/AlexanderKoch-Koch/low_cost_robot). GitHub repository.
- 670
671 Vikash Kumar. *Manipulators and Manipulation in high dimensional spaces*. PhD thesis, Uni-
672 versity of Washington, Seattle, 2016. URL [https://digital.lib.washington.edu/
673 researchworks/handle/1773/38104](https://digital.lib.washington.edu/researchworks/handle/1773/38104).
- 674
675 Zhiqi Li, Wenhai Wang, Hongyang Li, Enze Xie, Chonghao Sima, Tong Lu, Yu Qiao, and Jifeng Dai.
676 Bevformer: Learning bird’s-eye-view representation from multi-camera images via spatiotemporal
677 transformers. In *European conference on computer vision*, pp. 1–18. Springer, 2022.
- 678
679 Bo Liu, Yifeng Zhu, Chongkai Gao, Yihao Feng, Qiang Liu, Yuke Zhu, and Peter Stone. Libero:
680 Benchmarking knowledge transfer for lifelong robot learning. *Advances in Neural Information
681 Processing Systems*, 36, 2024.
- 682
683 Ilya Loshchilov, Frank Hutter, et al. Fixing weight decay regularization in adam. *arXiv preprint
684 arXiv:1711.05101*, 5, 2017.
- 685
686 Arjun Majumdar, Karmesh Yadav, Sergio Arnaud, Jason Ma, Claire Chen, Sneha Silwal, Aryan Jain,
687 Vincent-Pierre Berges, Tingfan Wu, Jay Vakil, et al. Where are we in the search for an artificial
688 visual cortex for embodied intelligence? *Advances in Neural Information Processing Systems*, 36:
689 655–677, 2023.
- 690
691 Arjun Majumdar, Anurag Ajay, Xiaohan Zhang, Pranav Putta, Sriram Yenamandra, Mikael Henaff,
692 Sneha Silwal, Paul Mcvay, Oleksandr Maksymets, Sergio Arnaud, et al. Openeqa: Embodied
693 question answering in the era of foundation models. In *Proceedings of the IEEE/CVF Conference
694 on Computer Vision and Pattern Recognition*, pp. 16488–16498, 2024.
- 695
696 Ben Mildenhall, Pratul P Srinivasan, Matthew Tancik, Jonathan T Barron, Ravi Ramamoorthi, and
697 Ren Ng. Nerf: Representing scenes as neural radiance fields for view synthesis. *Communications
698 of the ACM*, 65(1):99–106, 2021.
- 699
700 Suraj Nair, Aravind Rajeswaran, Vikash Kumar, Chelsea Finn, and Abhinav Gupta. R3m: A universal
701 visual representation for robot manipulation. *arXiv preprint arXiv:2203.12601*, 2022.
- 702
703 Maxime Oquab, Timothée Darcet, Théo Moutakanni, Huy Vo, Marc Szafraniec, Vasil Khalidov,
704 Pierre Fernandez, Daniel Haziza, Francisco Massa, Alaaeldin El-Nouby, et al. Dinov2: Learning
705 robust visual features without supervision. *arXiv preprint arXiv:2304.07193*, 2023.
- 706
707 Joseph Ortiz, Alexander Clegg, Jing Dong, Edgar Sucar, David Novotny, Michael Zollhoefer, and
708 Mustafa Mukadam. isdf: Real-time neural signed distance fields for robot perception. *arXiv
709 preprint arXiv:2204.02296*, 2022.

- 702 Xiaqing Pan, Nicholas Charron, Yongqian Yang, Scott Peters, Thomas Whelan, Chen Kong, Omkar
703 Parkhi, Richard Newcombe, and Yuheng Carl Ren. Aria digital twin: A new benchmark dataset
704 for egocentric 3d machine perception. In *Proceedings of the IEEE/CVF International Conference
705 on Computer Vision*, pp. 20133–20143, 2023.
- 706 Alec Radford, Jong Wook Kim, Chris Hallacy, Aditya Ramesh, Gabriel Goh, Sandhini Agarwal,
707 Girish Sastry, Amanda Askell, Pamela Mishkin, Jack Clark, et al. Learning transferable visual
708 models from natural language supervision. In *International conference on machine learning*, pp.
709 8748–8763. PMLR, 2021.
- 710 Ilija Radosavovic, Tete Xiao, Stephen James, Pieter Abbeel, Jitendra Malik, and Trevor Darrell.
711 Real-world robot learning with masked visual pre-training. In *Conference on Robot Learning*, pp.
712 416–426. PMLR, 2023.
- 713 René Ranftl, Katrin Lasinger, David Hafner, Konrad Schindler, and Vladlen Koltun. Towards
714 robust monocular depth estimation: Mixing datasets for zero-shot cross-dataset transfer. *IEEE
715 Transactions on Pattern Analysis and Machine Intelligence (TPAMI)*, 2020.
- 716 Mike Ranzinger, Greg Heinrich, Jan Kautz, and Pavlo Molchanov. Am-radio: Agglomerative vision
717 foundation model reduce all domains into one. In *Proceedings of the IEEE/CVF Conference on
718 Computer Vision and Pattern Recognition*, pp. 12490–12500, 2024.
- 719 Mike Roberts, Jason Ramapuram, Anurag Ranjan, Atulit Kumar, Miguel Angel Bautista, Nathan
720 Paczan, Russ Webb, and Joshua M Susskind. Hypersim: A photorealistic synthetic dataset for
721 holistic indoor scene understanding. In *Proceedings of the IEEE/CVF international conference on
722 computer vision*, pp. 10912–10922, 2021.
- 723 Jinghuan Shang, Karl Schmeckpeper, Brandon B. May, Maria Vittoria Minniti, Tarik Kelestemur,
724 David Watkins, and Laura Herlant. Theia: Distilling diverse vision foundation models for robot
725 learning. *arXiv*, 2024.
- 726 Wenzhe Shi, Jose Caballero, Ferenc Huszár, Johannes Totz, Andrew P Aitken, Rob Bishop, Daniel
727 Rueckert, and Zehan Wang. Real-time single image and video super-resolution using an efficient
728 sub-pixel convolutional neural network. In *Proceedings of the IEEE conference on computer vision
729 and pattern recognition*, pp. 1874–1883, 2016.
- 730 Mohit Shridhar, Lucas Manuelli, and Dieter Fox. Perceiver-actor: A multi-task transformer for
731 robotic manipulation. In *Conference on Robot Learning*, pp. 785–799. PMLR, 2023.
- 732 Leslie N Smith and Nicholay Topin. Super-convergence: Very fast training of neural networks using
733 large learning rates. In *Artificial intelligence and machine learning for multi-domain operations
734 applications*, volume 11006, pp. 369–386. SPIE, 2019.
- 735 Zhan Tong, Yibing Song, Jue Wang, and Limin Wang. Videomae: Masked autoencoders are data-
736 efficient learners for self-supervised video pre-training. *Advances in neural information processing
737 systems*, 35:10078–10093, 2022.
- 738 Saran Tunyasuvunakool, Alistair Muldal, Yotam Doron, Siqi Liu, Steven Bohez, Josh Merel, Tom
739 Erez, Timothy Lillicrap, Nicolas Heess, and Yuval Tassa. dm_control: Software and tasks for
740 continuous control. *Software Impacts*, 6:100022, 2020.
- 741 Chen Wang, Haochen Shi, Weizhuo Wang, Ruohan Zhang, Li Fei-Fei, and C Karen Liu. Dexcap:
742 Scalable and portable mocap data collection system for dexterous manipulation. *arXiv preprint
743 arXiv:2403.07788*, 2024a.
- 744 Chenxi Wang, Hongjie Fang, Hao-Shu Fang, and Cewu Lu. Rise: 3d perception makes real-world
745 robot imitation simple and effective. *arXiv preprint arXiv:2404.12281*, 2024b.
- 746 Jingwen Wang, Tymoteusz Bleja, and Lourdes Agapito. Go-surf: Neural feature grid optimization
747 for fast, high-fidelity rgb-d surface reconstruction. In *2022 International Conference on 3D Vision
748 (3DV)*, pp. 433–442. IEEE, 2022.

- 756 Letian Wang, Seung Wook Kim, Jiawei Yang, Cunjun Yu, Boris Ivanovic, Steven L Waslander, Yue
757 Wang, Sanja Fidler, Marco Pavone, and Peter Karkus. Distillnerf: Perceiving 3d scenes from
758 single-glance images by distilling neural fields and foundation model features. *arXiv preprint*
759 *arXiv:2406.12095*, 2024c.
- 760 Limin Wang, Bingkun Huang, Zhiyu Zhao, Zhan Tong, Yinan He, Yi Wang, Yali Wang, and Yu Qiao.
761 Videomae V2: scaling video masked autoencoders with dual masking. In *CVPR*, pp. 14549–14560,
762 2023.
- 763 Peng Wang, Lingjie Liu, Yuan Liu, Christian Theobalt, Taku Komura, and Wenping Wang. Neus:
764 Learning neural implicit surfaces by volume rendering for multi-view reconstruction. *arXiv*
765 *preprint arXiv:2106.10689*, 2021.
- 766 Philippe Weinzaepfel, Thomas Lucas, Vincent Leroy, Johann Cabon, Vaibhav Arora, Romain Brégier,
767 Gabriela Csurka, Leonid Antsfeld, Boris Chidlovskii, and Jérôme Revaud. CroCo v2: Improved
768 Cross-view Completion Pre-training for Stereo Matching and Optical Flow. In *ICCV*, 2023.
- 769 Manuel Wüthrich, Felix Widmaier, Felix Grimmering, Joel Akpo, Shruti Joshi, Vaibhav Agrawal,
770 Bilal Hammoud, Majid Khadiv, Miroslav Bogdanovic, Vincent Berenz, et al. Trifinger: An
771 open-source robot for learning dexterity. *arXiv preprint arXiv:2008.03596*, 2020.
- 772 Honghui Yang, Sha Zhang, Di Huang, Xiaoyang Wu, Haoyi Zhu, Tong He, Shixiang Tang, Heng-
773 shuang Zhao, Qibo Qiu, Binbin Lin, et al. Unipad: A universal pre-training paradigm for
774 autonomous driving. In *Proceedings of the IEEE/CVF Conference on Computer Vision and Pattern*
775 *Recognition*, pp. 15238–15250, 2024a.
- 776 Jiange Yang, Sheng Guo, Gangshan Wu, and Limin Wang. Comae: single model hybrid pre-training
777 on small-scale rgb-d datasets. In *Proceedings of the AAAI Conference on Artificial Intelligence*,
778 volume 37, pp. 3145–3154, 2023.
- 779 Jiange Yang, Bei Liu, Jianlong Fu, Bocheng Pan, Gangshan Wu, and Limin Wang. Spatiotemporal
780 predictive pre-training for robotic motor control. *arXiv preprint arXiv:2403.05304*, 2024b.
- 781 Denis Yarats, Rob Fergus, Alessandro Lazaric, and Lerrel Pinto. Mastering visual continuous control:
782 Improved data-augmented reinforcement learning. *arXiv preprint arXiv:2107.09645*, 2021.
- 783 Chandan Yeshwanth, Yueh-Cheng Liu, Matthias Nießner, and Angela Dai. Scannet++: A high-
784 fidelity dataset of 3d indoor scenes. In *Proceedings of the IEEE/CVF International Conference on*
785 *Computer Vision*, pp. 12–22, 2023.
- 786 Alex Yu, Ruilong Li, Matthew Tancik, Hao Li, Ren Ng, and Angjoo Kanazawa. Plenotrees for
787 real-time rendering of neural radiance fields. In *Proceedings of the IEEE/CVF International*
788 *Conference on Computer Vision*, pp. 5752–5761, 2021.
- 789 Tianhe Yu, Deirdre Quillen, Zhanpeng He, Ryan Julian, Karol Hausman, Chelsea Finn, and Sergey
790 Levine. Meta-world: A benchmark and evaluation for multi-task and meta reinforcement learning.
791 In *Conference on robot learning*, pp. 1094–1100. PMLR, 2020.
- 792 Yuanwen Yue, Anurag Das, Francis Engelmann, Siyu Tang, and Jan Eric Lenssen. Improving 2d
793 feature representations by 3d-aware fine-tuning. In *European Conference on Computer Vision*, pp.
794 57–74. Springer, 2025.
- 795 Yanjie Ze, Gu Zhang, Kangning Zhang, Chenyuan Hu, Muhan Wang, and Huazhe Xu. 3d diffusion
796 policy. *arXiv preprint arXiv:2403.03954*, 2024.
- 797 Sha Zhang, Jiajun Deng, Lei Bai, Houqiang Li, Wanli Ouyang, and Yanyong Zhang. Hvdistill:
798 Transferring knowledge from images to point clouds via unsupervised hybrid-view distillation.
799 *International Journal of Computer Vision*, pp. 1–15, 2024.
- 800 Tony Z Zhao, Vikash Kumar, Sergey Levine, and Chelsea Finn. Learning fine-grained bimanual
801 manipulation with low-cost hardware. *arXiv preprint arXiv:2304.13705*, 2023.

810 Jia Zheng, Junfei Zhang, Jing Li, Rui Tang, Shenghua Gao, and Zihan Zhou. Structured3d: A
811 large photo-realistic dataset for structured 3d modeling. In *Computer Vision–ECCV 2020: 16th*
812 *European Conference, Glasgow, UK, August 23–28, 2020, Proceedings, Part IX 16*, pp. 519–535.
813 Springer, 2020.

814 Haoyi Zhu, Hao-Shu Fang, and Cewu Lu. X-nerf: Explicit neural radiance field for multi-scene
815 360deg insufficient rgb-d views. In *Proceedings of the IEEE/CVF Winter Conference on Applica-*
816 *tions of Computer Vision*, pp. 5766–5775, 2023a.

817 Haoyi Zhu, Honghui Yang, Xiaoyang Wu, Di Huang, Sha Zhang, Xianglong He, Tong He, Heng-
818 shuang Zhao, Chunhua Shen, Yu Qiao, et al. Ponderv2: Pave the way for 3d foundataion model
819 with a universal pre-training paradigm. *arXiv preprint arXiv:2310.08586*, 2023b.

820 Haoyi Zhu, Yating Wang, Di Huang, Weicai Ye, Wanli Ouyang, and Tong He. Point cloud mat-
821 ters: Rethinking the impact of different observation spaces on robot learning. *arXiv preprint*
822 *arXiv:2402.02500*, 2024.

823 Xizhou Zhu, Weijie Su, Lewei Lu, Bin Li, Xiaogang Wang, and Jifeng Dai. Deformable DETR:
824 deformable transformers for end-to-end object detection. In *International Conference on Learning*
825 *Representations*, 2021.

826 Yuke Zhu, Josiah Wong, Ajay Mandlekar, Roberto Martín-Martín, Abhishek Joshi, Soroush Nasiriany,
827 and Yifeng Zhu. robosuite: A modular simulation framework and benchmark for robot learning.
828 *arXiv preprint arXiv:2009.12293*, 2020.

829
830
831
832
833
834
835
836
837
838
839
840
841
842
843
844
845
846
847
848
849
850
851
852
853
854
855
856
857
858
859
860
861
862
863

A ADDITIONAL RENDERING LOSSES

Here we detail the three additional rendering losses we have applied in Sec. 2.4.

Eikonal Regularization Loss. The Eikonal regularization loss, denoted as $\mathcal{L}_{\text{eikonal}}$, is a widely used loss function for the regularization of signed distance functions (SDFs) (Gropp et al., 2020). It is defined as:

$$\mathcal{L}_{\text{eikonal}} = \frac{1}{N_r N_p} \sum_{i=1}^{N_r} \sum_{j=1}^{N_p} (\|\nabla s(\mathbf{p}_{i,j})\| - 1)^2, \quad (9)$$

where $\nabla s(\mathbf{p}_{i,j})$ represents the gradient of the SDF s at the location $\mathbf{p}_{i,j}$. Since the SDF is a distance measure, $\mathcal{L}_{\text{eikonal}}$ encourages the gradients to have unit norm at the query point.

Near-Surface and Free Space Loss for SDF. To improve SDF estimation, we incorporate additional approximate SDF supervision, similar to iSDF (Ortiz et al., 2022) and GO-Surf (Wang et al., 2022). Specifically, for near-surface points, the difference between rendered depth and ground-truth depth serves as pseudo-SDF ground-truth supervision. For points far from the surface, a free space loss is used to further regularize the SDF values.

To compute the approximate SDF supervision, we define an indicator $b(z)$ for each sampled ray point with ray length z and corresponding ground-truth depth D :

$$b(z) = D - z. \quad (10)$$

The value $b(z)$ can be considered a credible approximate SDF value when it is small. Let t be a user-defined threshold, set to 0.05 in our experiments. For sampled ray points satisfying $b(z) \leq t$, we apply the near-surface SDF loss to constrain the SDF prediction $s(z_{i,j})$:

$$\mathcal{L}_{\text{sdf}} = \frac{1}{N_r N_p} \sum_{i=1}^{N_r} \sum_{j=1}^{N_p} |s(z_{i,j}) - b(z_{i,j})|. \quad (11)$$

For the remaining sampled ray points, we utilize a free space loss:

$$\mathcal{L}_{\text{free}} = \frac{1}{N_r N_p} \sum_{i=1}^{N_r} \sum_{j=1}^{N_p} \max\left(0, e^{-\alpha \cdot s(z_{i,j})} - 1, s(z_{i,j}) - b(z_{i,j})\right), \quad (12)$$

where α is set to 5, following Ortiz et al. (2022); Wang et al. (2022). Due to the presence of noisy depth images, \mathcal{L}_{sdf} and $\mathcal{L}_{\text{free}}$ are applied only to rays with valid depth values.

In our experiments, we adopt a similar weighting scheme to GO-Surf (Wang et al., 2022), setting $\lambda_C = 10.0$, $\lambda_D = 1.0$, $\lambda_{\text{sdf}} = 10.0$, and $\lambda_{\text{free}} = 1.0$. We observe that the Eikonal term can lead to overly smooth reconstructions, so we use a small weight of 0.01 for the Eikonal loss.

B EVALUATION SETUPS

Here we detail the setups of our large-scale evaluation in Sec. 3. For the detailed visualizations of each task, we recommend the readers to read the original simulator’s or benchmark’s dataset.

B.1 SINGLE-TASK BENCHMARKS

VC-1 (Majumdar et al., 2023). This benchmark includes several simulators. We selected four: Adroit (Kumar, 2016), Meta-World (Yu et al., 2020), DMControl (Tunyasuvunakool et al., 2020), and TriFinger (Wüthrich et al., 2020). The Adroit subset focuses on dexterous manipulation with 2 tasks: Relocate and Pen. The Meta-World subset addresses two-finger gripper manipulation with 5 tasks: Button Press Topdown, Drawer Open, Bin Picking, Hammer, and Assembly. The DMControl subset is for locomotion control, also with 5 tasks: Walker Stand, Walker Walk,

918 **Reacher Easy, Cheetah Run, and Finger Spin.** The TriFinger subset targets three-finger
 919 manipulation with 2 tasks: **Reach Cube and Move Cube.** For all tasks, we use a 3-layer MLP
 920 as the policy network for each single-task training, following the original implementation. Each
 921 task is trained with 100 demonstrations, except for 25 on Meta-World, and evaluated 50 times using
 922 the specific seeds 100, 200, and 300. The [CLS] token of a frozen pre-trained ViT is used as the
 923 observation feature. All hyper-parameters are kept the same with the original implementation.

924 **Franka Kitchen (Gupta et al., 2019).** Franka-Kitchen is a MuJoCo-modeled simulation environment
 925 with a Franka robot in a kitchen scene. Its action space is the 9-dimensional joint velocity with 7
 926 DoF for the arm and 2 DoF for the gripper. Following previous works (Nair et al., 2022; Karamcheti
 927 et al., 2023), we evaluate five tasks: **Sliding Door, Turning Light On, Opening Door,**
 928 **Turning Knob, and Opening Microwave.** Each task spans two camera viewpoints and three
 929 random seeds. Similar to the evaluation scheme in VC-1, we utilize 25 demonstrations to train a
 930 policy model, which is a 2-layer MLP with hidden sizes [256, 256] preceded by a BatchNorm.

931 **Meta-World (Yu et al., 2020).** This benchmark comprises a series of tasks in which an agent
 932 directs a Sawyer robot arm to manipulate objects in a tabletop environment. We selected 48 tasks,
 933 encompassing easy, medium, and hard levels. We implemented the Diffusion Policy (Chi et al., 2023)
 934 on this benchmark and adhered to the setup in Ze et al. (2024) to generate 10 demonstrations for
 935 each single-task training, followed by evaluation through 20 rollouts. The average results across
 936 three fixed seeds (100, 200, 300) are reported. The [CLS] token from a frozen pre-trained ViT
 937 serves as the observation feature. **The 48 tasks include: Button Press Wall, Door Close,**
 938 **Door Unlock, Drawer Close, Drawer Open, Faucet Close, Plate Slide, Plate**
 939 **Slide Back, Plate Slide Side, Window Close, Basketball, Bin Picking, Box**
 940 **Close, Coffee Push, Assembly, Disassemble, Push Wall, Shelf Place, Door**
 941 **Open, Button Press, Sweep Into, Door Lock, Reach Wall, Hammer, Stick**
 942 **Push, Button Press Topdown, Handle Press Side, Plate Slide Back Side,**
 943 **Sweep, Button Press Topdown Wall, Handle Press, Push, Coffee Pull, Dial**
 944 **Turn, Reach, Coffee Button, Pick Place Wall, Stick Pull, Hand Insert, Peg**
 945 **Insert Side, Pick Place, Faucet Open, Push Back, Lever Pull, Handle Pull,**
 946 **Soccer, Window Open, and Pick Out Of Hole.**

947 B.2 LANGUAGE-CONDITIONED MULTI-TASK BENCHMARKS

949 **RLBench (James et al., 2020).** This benchmark is a prominent language-conditioned multi-task
 950 robot learning framework. PolarNet (Chen et al., 2023) has categorized all tasks into 9 groups. We
 951 selected 71 tasks from RLBench that can be successfully executed and split them into two groups
 952 uniformly on categories: Group 1 with 35 tasks and Group 2 with 36 tasks. Each task includes 100
 953 training demonstrations and 25 testing rollouts. For each group, we train a language-conditioned
 954 multi-task agent. We employ RVT-2 (Goyal et al., 2024), the state-of-the-art (SOTA) method on
 955 this benchmark, as our policy. RVT-2 takes multiple images rendered from point clouds as inputs
 956 and uses a convolutional block to generate feature maps. We substitute the convolutional block with
 957 different pre-trained ViTs, unpatchifying the latent vectors concatenated with the global [CLS]
 958 token to obtain feature maps. All other architectures and hyperparameters remain consistent with the
 959 original RVT-2 implementation.

960 **The 35 tasks in Group 1 include: Basketball In Hoop, Put Rubbish In Bin, Meat**
 961 **Off Grill, Meat On Grill, Slide Block To Target, Reach And Drag, Take**
 962 **Frame Off Hanger, Water Plants, Hang Frame On Hanger, Wipe Desk, Stack**
 963 **Blocks, Reach Target, Push Button, Lamp On, Toilet Seat Down, Close**
 964 **Laptop Lid, Open Box, Open Drawer, Pick Up Cup, Turn Tap, Take Usb Out**
 965 **Of Computer, Play Jenga, Insert Onto Square Peg, Take Umbrella Out Of**
 966 **Umbrella Stand, Insert Usb In Computer, Straighten Rope, Turn Oven On,**
 967 **Change Clock, Close Microwave, Close Fridge, Close Grill, Open Grill,**
 968 **Unplug Charger, Press Switch, and Take Money Out Safe.**

969 **The 36 tasks in Group 2 include: Change Channel, Tv On, Push Buttons, Stack**
 970 **Wine, Scoop With Spatula, Place Hanger On Rack, Move Hanger, Sweep To**
 971 **Dustpan, Take Plate Off Colored Dish Rack, Screw Nail, Take Shoes Out**
Of Box, Slide Cabinet Open And Place Cups, Lamp Off, Pick And Lift,

972 Take Lid Off Saucepan, Close Drawer, Close Box, Phone On Base, Toilet
 973 Seat Up, Put Books On Bookshelf, Beat The Buzz, Stack Cups, Put Knife
 974 On Chopping Board, Place Shape In Shape Sorter, Take Toilet Roll Off
 975 Stand, Put Umbrella In Umbrella Stand, Setup Checkers, Open Window,
 976 Open Wine Bottle, Open Microwave, Put Money In Safe, Open Door, Close
 977 Door, Open Fridge, Open Oven, and Plug Charger In Power Supply.

978 **LIBERO (Liu et al., 2024)**. Built upon Robosuite (Zhu et al., 2020), LIBERO (Liu et al., 2024)
 979 generates a total of 130 language-conditioned tasks across five suites: LIBERO-Spatial, LIBERO-
 980 Object, LIBERO-Goal, LIBERO-10, and LIBERO-90. Each suite contains 10 tasks, except for
 981 LIBERO-90, which includes 90 tasks. We train a language-conditioned multi-task policy for each
 982 suite, adopting the transformer policy provided by LIBERO. The image encoders are modified from
 983 default CNNs to frozen pre-trained ViTs, utilizing the [CLS] token for feature extraction. To
 984 expedite policy training, we use only 20 demonstrations per task and forgo augmentations, allowing
 985 for pre-extraction of all image features during training. After training for 25 epochs, the checkpoints
 986 from the 20th and 25th are evaluated with 20 rollouts per task, and the best checkpoint’s performance
 987 is taken. Finally, the results are averaged on 3 random seeds.

988 The 10 tasks in LIBERO-Spatial are:

- 989 1. Pick up the black bowl between the plate and the ramekin and place it on the plate.
- 990 2. Pick up the black bowl next to the ramekin and place it on the plate.
- 991 3. Pick up the black bowl from table center and place it on the plate.
- 992 4. Pick up the black bowl on the cookie box and place it on the plate.
- 993 5. Pick up the black bowl in the top drawer of the wooden cabinet and place it on the plate.
- 994 6. Pick up the black bowl on the ramekin and place it on the plate.
- 995 7. Pick up the black bowl next to the cookie box and place it on the plate.
- 996 8. Pick up the black bowl on the stove and place it on the plate.
- 997 9. Pick up the black bowl next to the plate and place it on the plate.
- 998 10. Pick up the black bowl on the wooden cabinet and place it on the plate.

999 The 10 tasks in LIBERO-Object are:

- 1000 1. Pick up the alphabet soup and place it in the basket.
- 1001 2. Pick up the cream cheese and place it in the basket.
- 1002 3. Pick up the salad dressing and place it in the basket.
- 1003 4. Pick up the BBQ sauce and place it in the basket.
- 1004 5. Pick up the ketchup and place it in the basket.
- 1005 6. Pick up the tomato sauce and place it in the basket.
- 1006 7. Pick up the butter and place it in the basket.
- 1007 8. Pick up the milk and place it in the basket.
- 1008 9. Pick up the chocolate pudding and place it in the basket.
- 1009 10. Pick up the orange juice and place it in the basket.

1010 The 10 tasks in LIBERO-Goal are:

- 1011 1. Open the middle drawer of the cabinet.
- 1012 2. Put the bowl on the stove.
- 1013 3. Put the wine bottle on top of the cabinet.
- 1014 4. Open the top drawer and put the bowl inside.
- 1015 5. Put the bowl on top of the cabinet.
- 1016 6. Push the plate to the front of the stove.
- 1017 7. Put the cream cheese in the bowl.
- 1018 8. Turn on the stove.
- 1019 9. Put the bowl on the plate.
- 1020 10. Put the wine bottle on the rack.

1021 The 10 tasks in LIBERO-10 are:

- 1022 1. LIVING ROOM SCENE2: Put both the alphabet soup and the tomato sauce in the basket.
- 1023 2. LIVING ROOM SCENE2: Put both the cream cheese box and the butter in the basket.
- 1024 3. KITCHEN SCENE3: Turn on the stove and put the moka pot on it.
- 1025 4. KITCHEN SCENE4: Put the black bowl in the bottom drawer of the cabinet and close it.
- 1026 5. LIVING ROOM SCENE5: Put the white mug on the left plate and put the yellow and white mug
 on the right plate.

- 1026 6. STUDY SCENE1: Pick up the book and place it in the back compartment of the caddy.
1027 7. LIVING ROOM SCENE6: Put the white mug on the plate and put the chocolate pudding to the
1028 right of the plate.
1029 8. LIVING ROOM SCENE1: Put both the alphabet soup and the cream cheese box in the basket.
1030 9. KITCHEN SCENE8: Put both moka pots on the stove.
1031 10. KITCHEN SCENE6: Put the yellow and white mug in the microwave and close it.
- 1032 The 10 tasks in LIBERO-90 are:
1033 1. KITCHEN SCENE10: Close the top drawer of the cabinet.
1034 2. KITCHEN SCENE10: Close the top drawer of the cabinet and put the black bowl on top of it.
1035 3. KITCHEN SCENE10: Put the black bowl in the top drawer of the cabinet.
1036 4. KITCHEN SCENE10: Put the butter at the back in the top drawer of the cabinet and close it.
1037 5. KITCHEN SCENE10: Put the butter at the front in the top drawer of the cabinet and close it.
1038 6. KITCHEN SCENE10: Put the chocolate pudding in the top drawer of the cabinet and close it.
1039 7. KITCHEN SCENE1: Open the bottom drawer of the cabinet.
1040 8. KITCHEN SCENE1: Open the top drawer of the cabinet.
1041 9. KITCHEN SCENE1: Open the top drawer of the cabinet and put the bowl in it.
1042 10. KITCHEN SCENE1: Put the black bowl on the plate.
1043 11. KITCHEN SCENE1: Put the black bowl on top of the cabinet.
1044 12. KITCHEN SCENE2: Open the top drawer of the cabinet.
1045 13. KITCHEN SCENE2: Put the black bowl at the back on the plate.
1046 14. KITCHEN SCENE2: Put the black bowl at the front on the plate.
1047 15. KITCHEN SCENE2: Put the middle black bowl on the plate.
1048 16. KITCHEN SCENE2: Put the middle black bowl on top of the cabinet.
1049 17. KITCHEN SCENE2: Stack the black bowl at the front on the black bowl in the middle.
1050 18. KITCHEN SCENE2: Stack the middle black bowl on the back black bowl.
1051 19. KITCHEN SCENE3: Put the frying pan on the stove.
1052 20. KITCHEN SCENE3: Put the moka pot on the stove.
1053 21. KITCHEN SCENE3: Turn on the stove.
1054 22. KITCHEN SCENE3: Turn on the stove and put the frying pan on it.
1055 23. KITCHEN SCENE4: Close the bottom drawer of the cabinet.
1056 24. KITCHEN SCENE4: Close the bottom drawer of the cabinet and open the top drawer.
1057 25. KITCHEN SCENE4: Put the black bowl in the bottom drawer of the cabinet.
1058 26. KITCHEN SCENE4: Put the black bowl on top of the cabinet.
1059 27. KITCHEN SCENE4: Put the wine bottle in the bottom drawer of the cabinet.
1060 28. KITCHEN SCENE4: Put the wine bottle on the wine rack.
1061 29. KITCHEN SCENE5: Close the top drawer of the cabinet.
1062 30. KITCHEN SCENE5: Put the black bowl in the top drawer of the cabinet.
1063 31. KITCHEN SCENE5: Put the black bowl on the plate.
1064 32. KITCHEN SCENE5: Put the black bowl on top of the cabinet.
1065 33. KITCHEN SCENE5: Put the ketchup in the top drawer of the cabinet.
1066 34. KITCHEN SCENE6: Close the microwave.
1067 35. KITCHEN SCENE6: Put the yellow and white mug to the front of the white mug.
1068 36. KITCHEN SCENE7: Open the microwave.
1069 37. KITCHEN SCENE7: Put the white bowl on the plate.
1070 38. KITCHEN SCENE7: Put the white bowl to the right of the plate.
1071 39. KITCHEN SCENE8: Put the right moka pot on the stove.
1072 40. KITCHEN SCENE8: Turn off the stove.
1073 41. KITCHEN SCENE9: Put the frying pan on the cabinet shelf.
1074 42. KITCHEN SCENE9: Put the frying pan on top of the cabinet.
1075 43. KITCHEN SCENE9: Put the frying pan under the cabinet shelf.
1076 44. KITCHEN SCENE9: Put the white bowl on top of the cabinet.
1077 45. KITCHEN SCENE9: Turn on the stove.
1078 46. KITCHEN SCENE9: Turn on the stove and put the frying pan on it.
1079 47. LIVING ROOM SCENE1: Pick up the alphabet soup and put it in the basket.
48. LIVING ROOM SCENE1: Pick up the cream cheese box and put it in the basket.
49. LIVING ROOM SCENE1: Pick up the ketchup and put it in the basket.
50. LIVING ROOM SCENE1: Pick up the tomato sauce and put it in the basket.
51. LIVING ROOM SCENE2: Pick up the alphabet soup and put it in the basket.

- 1080 52. LIVING ROOM SCENE2: Pick up the butter and put it in the basket.
 1081 53. LIVING ROOM SCENE2: Pick up the milk and put it in the basket.
 1082 54. LIVING ROOM SCENE2: Pick up the orange juice and put it in the basket.
 1083 55. LIVING ROOM SCENE2: Pick up the tomato sauce and put it in the basket.
 1084 56. LIVING ROOM SCENE3: Pick up the alphabet soup and put it in the tray.
 1085 57. LIVING ROOM SCENE3: Pick up the butter and put it in the tray.
 1086 58. LIVING ROOM SCENE3: Pick up the cream cheese and put it in the tray.
 1087 59. LIVING ROOM SCENE3: Pick up the ketchup and put it in the tray.
 1088 60. LIVING ROOM SCENE3: Pick up the tomato sauce and put it in the tray.
 1089 61. LIVING ROOM SCENE4: Pick up the black bowl on the left and put it in the tray.
 1090 62. LIVING ROOM SCENE4: Pick up the chocolate pudding and put it in the tray.
 1091 63. LIVING ROOM SCENE4: Pick up the salad dressing and put it in the tray.
 1092 64. LIVING ROOM SCENE4: Stack the left bowl on the right bowl and place them in the tray.
 1093 65. LIVING ROOM SCENE4: Stack the right bowl on the left bowl and place them in the tray.
 1094 66. LIVING ROOM SCENE5: Put the red mug on the left plate.
 1095 67. LIVING ROOM SCENE5: Put the red mug on the right plate.
 1096 68. LIVING ROOM SCENE5: Put the white mug on the left plate.
 1097 69. LIVING ROOM SCENE5: Put the yellow and white mug on the right plate.
 1098 70. LIVING ROOM SCENE6: Put the chocolate pudding to the left of the plate.
 1099 71. LIVING ROOM SCENE6: Put the chocolate pudding to the right of the plate.
 1100 72. LIVING ROOM SCENE6: Put the red mug on the plate.
 1101 73. LIVING ROOM SCENE6: Put the white mug on the plate.
 1102 74. STUDY SCENE1: Pick up the book and place it in the front compartment of the caddy.
 1103 75. STUDY SCENE1: Pick up the book and place it in the left compartment of the caddy.
 1104 76. STUDY SCENE1: Pick up the book and place it in the right compartment of the caddy.
 1105 77. STUDY SCENE1: Pick up the yellow and white mug and place it to the right of the caddy.
 1106 78. STUDY SCENE2: Pick up the book and place it in the back compartment of the caddy.
 1107 79. STUDY SCENE2: Pick up the book and place it in the front compartment of the caddy.
 1108 80. STUDY SCENE2: Pick up the book and place it in the left compartment of the caddy.
 1109 81. STUDY SCENE2: Pick up the book and place it in the right compartment of the caddy.
 1110 82. STUDY SCENE3: Pick up the book and place it in the front compartment of the caddy.
 1111 83. STUDY SCENE3: Pick up the book and place it in the left compartment of the caddy.
 1112 84. STUDY SCENE3: Pick up the book and place it in the right compartment of the caddy.
 1113 85. STUDY SCENE3: Pick up the red mug and place it to the right of the caddy.
 1114 86. STUDY SCENE3: Pick up the white mug and place it to the right of the caddy.
 1115 87. STUDY SCENE4: Pick up the book in the middle and place it on the cabinet shelf.
 1116 88. STUDY SCENE4: Pick up the book on the left and place it on top of the shelf.
 1117 89. STUDY SCENE4: Pick up the book on the right and place it on the cabinet shelf.
 1118 90. STUDY SCENE4: Pick up the book on the right and place it under the cabinet shelf.

1118 C MORE IMPLEMENTATION DETAILS

1119 C.1 DATASET DETAILS

1120 The datasets used for SPA include ScanNet, ScanNet++, Hypersim, ADT, S3DIS, and Droid.

1121 **ScanNet** consists of 1.89 million frames in total. Each epoch includes 1.5 times the dataset size. For
 1122 each scene, a random starting frame is selected, followed by the sampling of 1 to 8 frames at random,
 1123 with an interval of 8 frames between them.

1124 **ScanNet++** comprises 0.11 million frames. Each epoch includes 5 times the dataset size. For each
 1125 scene, a random starting frame is selected, followed by the sampling of 1 to 8 frames at random, with
 1126 an interval of 5 frames between them.

1127 **Hypersim** contains 0.03 million frames. Each epoch includes 8 times the dataset size. For each
 1128 scene, we randomly select 1 to 8 continuous frames.

1129 **ADT** consists of 0.0015M frames in total. Each epoch includes 1 times the dataset size. For each
 1130 scene, 1 to 8 continuous frames are randomly selected.

S3DIS consists of 0.015 million frames. Each epoch includes 5 times the dataset size. For each scene, a random starting frame is selected, followed by the sampling of 1 to 8 frames at random, with an interval of 5 frames between them.

Droid contains a large number of videos, but due to the high similarity between frames, the videos are first downsampled by a factor of 15 during pre-processing, resulting in 1.78 million frames. Since Droid does not provide depth data, we utilize Croco-Stereo [Weinzaepfel et al. \(2023\)](#) to estimate dense depth maps for rendering supervision. Additionally, due to the significant noise in the camera pose data, only a single frame is sampled at a time during training.

During pre-training, we first resize the multi-view input images to slightly larger than 224×224 , and then randomly crop them to a final size of 224×224 . Random photometric distortions with a probability of 0.5 are applied for augmentation, including brightness ranging from 0.875 to 1.125, contrast ranging from 0.5 to 1.5, saturation ranging from 0.5 to 1.5, and hue ranging from -0.05 to 0.05. Frames with very small valid depth areas or scene boxes are filtered out.

For semantic rendering supervision, we observe that using larger image sizes improves the quality of feature maps generated by RADIO. Consequently, we resize the images to 1024×1024 before feeding them into RADIO, which outputs a feature map of size 64×64 . We then apply bilinear sampling to query the semantic feature labels for each pixel.

C.2 PRE-TRAINING DETAILS

For stability during pre-training, we apply the Exponential Moving Average (EMA) with a decay rate of 0.999. The model is trained for 2000 epochs on 80 NVIDIA A100-80G GPUs, using a gradient clipping threshold of 1.0. Each GPU processes a batch size of 2, with 8 gradient accumulation steps, resulting in a total effective batch size of $2 \times 80 \times 8 = 1280$. We employ the AdamW optimizer with a weight decay of 0.04. The base learning rate is set to 5×10^{-6} , and the actual learning rate is scaled by a factor of 8 times the effective batch size. A OneCycle learning rate scheduler is used, with a percentage start of 0.05, a divide factor of 100, and a final divide factor of 1000.

To facilitate faster convergence and improve stability, we initialize the encoder with ImageNet pre-trained weights from the Masked Autoencoder (MAE), applying a learning rate layer decay of 0.8. This initialization does not affect the validity of our conclusions, as demonstrated by the ablation study of SPA-MAE in Sec. 5.3. The ViT encoder and upsampling layers are trained with FP16 precision, while the volume decoder is trained with FP32 precision.

We set the loss weights to $\lambda_{\text{color}} = 10$, $\lambda_{\text{depth}} = 1$, $\lambda_{\text{semantic}} = 1$, $\lambda_{\text{eikonal}} = 0.01$, $\lambda_{\text{free}} = 1$, and $\lambda_{\text{sdf}} = 10$. For the NeuS sampler, the initial number of samples is set to 72, with 24 importance samples. In each iteration, we randomly sample 512 pixels per view for rendering and supervision.

D DETAILED RESULTS OF EACH TASK

We present the results of all individual tasks in Tab. 12, Tab. 13, Tab. 14, Tab. 15, Tab. 16, and Tab. 17.

E CAMERA POSE ESTIMATION DETAILS

We adopt a setup similar to that of [El Banani et al. \(2024\)](#) for camera pose estimation using the NAVI dataset ([Jampani et al., 2023](#)). Given an image pair from different viewpoints, we first extract features from each image using a frozen, pre-trained Vision Transformer (ViT) encoder. Following standard protocols for embodied evaluation, we use the [CLS] token as the feature representation. The two [CLS] tokens are then concatenated and passed through a BatchNorm layer and a Multi-Layer Perceptron (MLP) to regress the camera pose. The MLP consists of four linear layers with three ReLU activations, using hidden sizes of 512, 256, and 128 units, and outputs a 7-dimensional pose vector. The first three dimensions represent the xyz translation, while the last four dimensions correspond to the rotation quaternions.

We employ the Mean Squared Error (MSE) loss function and optimize the model using the AdamW optimizer with a OneCycle learning rate scheduler. The model is trained for 100 epochs with a base learning rate of 1×10^{-3} and a starting percentage of 0.1. For evaluation, we use Euclidean distance

as the translation error metric and geodesic distance as the rotation error metric. The geodesic distance between two quaternions q_1 and q_2 is defined as:

$$\theta = 2 \cdot \arccos(|q_1 \cdot q_2|), \quad (13)$$

where q_1 and q_2 are normalized quaternions, and \cdot denotes the quaternion dot product. The Euclidean distance d between two translation vectors $\mathbf{t}_1 = (x_1, y_1, z_1)$ and $\mathbf{t}_2 = (x_2, y_2, z_2)$ is given by:

$$d = \sqrt{(x_2 - x_1)^2 + (y_2 - y_1)^2 + (z_2 - z_1)^2}. \quad (14)$$

F REAL-WORLD EXPERIMENT DETAILS

Our real-world hardware setup is based on the open-source Low-Cost-Robot project (Koch, 2024). We utilize two Intel RealSense D415 cameras for image capture. A visualization of our platform is provided in Fig. 8. For teleoperation, policy training, and evaluation, we leverage the open-source RealRobot project (Contributors, 2024). The policy used is the ACT policy (Zhao et al., 2023).

For each task, we collect 50 demonstrations, and during evaluation, we conduct 25 rollouts, each with randomized object locations and orientations. The model is trained for 10,000 epochs using four NVIDIA A100 GPUs. We employ the AdamW optimizer with a learning rate of 5×10^{-5} and a weight decay of 0.05. Additionally, a OneCycle learning rate scheduler is used, with a starting percentage of 0.1, a division factor of 10, and a final division factor of 100.

G ADDITIONAL REINFORCEMENT LEARNING EXPERIMENTS

We conduct additional RL experiments following the settings in Hu et al. (2023) to use DrQ-v2 (Yarats et al., 2021), a state-of-the-art off-policy actor-critic approach for continuous vision-based control. We train some RL experiments with different pre-trained vision representations with ViT-Base architectures. The vision encoders are frozen during RL training. Five tasks in the Meta-World benchmark are chosen, as shown below. We train for a total of 1.1M frames and all other hyper-parameters including random seeds are kept as default and same. We run three seeds for each experiment. We report the evaluation success rate and episode reward below in Tab. 9. The reward curves are visualized in Fig. 7. From the results, it is evident that the reinforcement learning outcomes exhibit high variance. Nevertheless, overall, our 3D spatial-aware representation outperforms other representation learning methods.

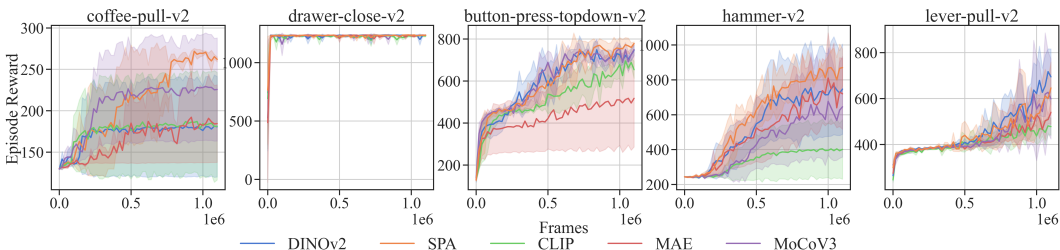


Figure 7: Reinforcement learning reward curves visualization.

H ADDITIONAL MONOCULAR GRASP POSE DETECTION EXPERIMENTS

We conduct a monocular grasp pose detection experiment to further investigate more complex robotics learning paradigms. We follow similar settings in Gou et al. (2021), which train a neural network to detect the 7-DoF grasp poses on monocular image observations. The experiment is conducted on GraspNet-1Billion (Fang et al., 2020), a large-scale real-world object grasping benchmark. We follow the hyper-parameters and setups in the official implementation, except that we replace the default ResNet with different pre-trained ViT models for feature extraction. All pre-trained representations are with ViT-Base architecture and are frozen during training. We report the overall Top-K accuracy on the test set below. The results align well with our findings and indicate that SPA also outperforms other representation learning methods in the monocular grasp pose detection task.

Table 9: Reinforcement learning comparison results.

Meta-World RL Task	Method (ViT-B)	Success Rate	Episode Reward
button-press-topdown-v2	CLIP	0.93	653.97
	DINOv2	1.00	746.04
	MAE	0.46	517.54
	MoCoV3	0.99	749.93
	SPA (Ours)	1.00	778.47
hammer-v2	CLIP	0.00	401.41
	DINOv2	0.67	746.74
	MAE	0.66	720.19
	MoCoV3	0.59	645.46
	SPA (Ours)	1.00	870.32
lever-pull-v2	CLIP	0.00	478.18
	DINOv2	0.00	694.73
	MAE	0.00	540.44
	MoCoV3	0.23	598.54
	SPA (Ours)	0.15	646.33
coffee-pull-v2	CLIP	0.00	181.40
	DINOv2	0.00	180.72
	MAE	0.00	184.56
	MoCoV3	0.00	225.73
	SPA (Ours)	0.00	262.11
drawer-close-v2	CLIP	1.00	1228.90
	DINOv2	1.00	1236.30
	MAE	1.00	1233.91
	MoCoV3	1.00	1233.46
	SPA (Ours)	1.00	1235.81
Mean	CLIP	0.39	588.77
	DINOv2	0.53	720.91
	MAE	0.42	639.33
	MoCoV3	0.56	690.63
	SPA (Ours)	0.63	758.61

Table 10: Overall top-k monocular grasp pose detection accuracy of various methods (ViT-Base).

Method (ViT-Base)	CLIP	DINOv2	MoCoV3	MAE	SPA
Overall Accuracy	21.10	22.08	29.39	31.03	31.20

I ADDITIONAL ABLATION STUDY ON NEURAL RENDERING

To clarify the contribution of neural rendering to the overall performance of SPA, we conducted an additional ablation study. In this study, we maintained all settings identical—data loading, training techniques, hyperparameters, and the encoder—while replacing the volume neural rendering decoder with a multiview transformer-based decoder, similar to the MAE decoder. This alternative decoder receives masked patches filled with mask tokens corresponding to multiview images. Additional camera pose embeddings are added, and attention layers are used to fuse the multiview information and reconstruct RGB and depth images. We refer to this baseline as MV-MAE. It was trained on the ScanNet dataset without semantic supervision, ensuring a fair comparison with the result in the last line of Tab. 7. The results from this experiment demonstrate that neural rendering is crucial for incorporating explicit 3D spatial information. Simple multiview attention-based interaction, as used in MV-MAE, does not perform as effectively in learning 3D spatial awareness.

Table 11: Additional Ablation Study on Neural Rendering. The models are evaluated on two subsets of the VC-1 benchmark. The model architectures are both ViT-base.

Method	Meta-World	DMControl
MV-MAE	84.8±5.8	59.6±3.2
SPA	88.0±4.5	61.5±3.4

Table 12: All results on Vc-1 benchmarks.

Benchmark		AD		MW				DMC				TF			
Methods	Seed	Relocate	Pen	Button Press Topdown	Drawer Open	Bin Picking	Hammer	Assembly	Walker Stand	Walker Walk	Reacher Easy	Cheetah Run	Finger Spin	Reach Cube	Move Cube
<i>ViT-L Methods</i>															
MoCoV3	100	40.00	92.00	88.00	100.00	88.00	100.00	88.00	84.88	57.59	92.29	56.28	70.49	84.37	61.20
	200	36.00	80.00	88.00	100.00	80.00	100.00	84.00	82.95	55.02	92.08	43.17	69.49	84.20	61.26
	300	28.00	76.00	84.00	100.00	68.00	92.00	72.00	81.42	53.59	91.96	41.27	68.23	84.09	64.24
MAE	100	36.00	84.00	84.00	100.00	88.00	100.00	100.00	951.27	680.69	976.50	482.47	703.30	85.46	59.46
	200	36.00	80.00	84.00	100.00	76.00	96.00	96.00	933.67	676.92	952.20	49.22	695.00	86.88	59.45
	300	32.00	80.00	68.00	100.00	72.00	98.00	88.00	873.53	659.41	895.60	501.91	691.80	85.26	61.69
DINOv2	100	32.00	68.00	68.00	100.00	84.00	100.00	88.00	87.01	56.52	94.50	26.98	70.87	86.16	50.84
	200	28.00	68.00	60.00	100.00	80.00	96.00	80.00	86.00	53.97	89.97	21.84	68.78	86.87	50.78
	300	28.00	60.00	60.00	100.00	80.00	92.00	72.00	82.41	51.69	88.36	21.34	67.41	86.05	50.17
CLIP	100	24.00	80.00	28.00	100.00	88.00	100.00	84.00	66.16	43.94	90.71	18.40	68.30	73.28	41.09
	200	24.00	72.00	24.00	100.00	84.00	100.00	80.00	64.04	34.51	88.26	16.52	66.68	75.11	33.45
	300	24.00	68.00	16.00	100.00	84.00	96.00	72.00	52.70	31.60	85.17	14.51	67.49	74.73	38.95
EVA	100	44.00	84.00	72.00	100.00	76.00	100.00	100.00	77.92	51.64	98.17	31.04	70.17	82.56	52.04
	200	40.00	76.00	84.00	100.00	72.00	100.00	100.00	77.63	50.81	86.66	19.37	67.43	81.72	52.07
	300	32.00	72.00	96.00	100.00	68.00	96.00	96.00	77.21	47.71	88.41	29.19	67.43	82.13	52.70
InternViT-300M	100	40.00	72.00	80.00	100.00	72.00	100.00	84.00	70.04	30.44	80.80	16.70	67.05	78.59	53.67
	200	28.00	72.00	68.00	100.00	76.00	96.00	84.00	67.63	31.55	82.33	19.39	67.57	77.07	55.21
	300	28.00	80.00	60.00	100.00	72.00	96.00	72.00	66.95	29.28	81.87	18.80	68.55	78.27	48.58
InternViT-6B	100	32.00	72.00	88.00	100.00	80.00	100.00	84.00	88.53	70.02	93.09	26.54	70.62	85.96	57.52
	200	40.00	76.00	84.00	100.00	76.00	100.00	80.00	85.28	60.09	90.86	22.84	69.04	86.30	54.11
	300	60.00	80.00	80.00	100.00	88.00	100.00	76.00	81.88	59.17	87.87	21.53	67.20	85.68	54.86
MVP	100	32.00	84.00	96.00	100.00	96.00	100.00	100.00	84.88	57.59	92.29	56.28	70.49	84.37	61.20
	200	28.00	76.00	92.00	100.00	84.00	100.00	96.00	82.95	55.02	92.08	43.17	69.49	84.20	61.26
	300	24.00	76.00	84.00	100.00	68.00	100.00	88.00	81.42	53.59	91.96	41.27	68.23	84.09	64.24
VC-1	100	32.00	84.00	84.00	100.00	76.00	96.00	96.00	82.36	55.33	98.09	35.31	72.60	83.36	58.00
	200	28.00	80.00	68.00	100.00	72.00	92.00	84.00	80.21	53.90	89.83	34.10	70.15	83.17	61.00
	300	24.00	76.00	76.00	100.00	96.00	88.00	84.00	68.62	50.13	87.89	31.18	70.11	82.75	57.16
SPA-L	100	40.00	88.00	76.00	100.00	92.00	100.00	100.00	94.19	66.34	95.57	52.53	73.95	87.37	56.68
	200	44.00	76.00	84.00	100.00	88.00	100.00	84.00	92.28	60.60	81.43	44.99	71.83	87.26	64.35
	300	36.00	76.00	96.00	100.00	88.00	96.00	96.00	87.87	51.75	83.86	39.10	70.91	87.62	58.02
<i>ViT-B Methods and Others</i>															
STP-B	100	20.00	80.00	88.00	100.00	84.00	100.00	96.00	77.02	45.34	87.97	40.01	72.72	80.41	54.66
	200	28.00	76.00	92.00	100.00	84.00	100.00	80.00	71.50	33.60	84.08	34.30	72.18	80.13	57.97
	300	32.00	76.00	88.00	100.00	72.00	100.00	96.00	71.44	42.86	79.67	39.17	69.12	80.65	53.95
R3M-B	100	20.00	92.00	52.00	96.00	32.00	88.00	48.00	668.49	301.54	842.90	256.56	678.00	75.08	45.66
	200	12.00	76.00	48.00	96.00	32.00	88.00	44.00	634.62	256.82	661.40	198.63	660.90	75.62	48.09
	300	12.00	76.00	32.00	88.00	28.00	76.00	40.00	633.39	211.90	585.50	188.15	657.30	74.54	45.59
Theia-B	100	32.00	76.00	88.00	100.00	80.00	96.00	96.00	72.90	43.97	82.09	37.02	70.50	84.55	55.62
	200	36.00	80.00	60.00	100.00	84.00	100.00	84.00	79.05	56.99	94.36	39.59	70.22	83.27	54.59
	300	24.00	72.00	80.00	100.00	72.00	96.00	100.00	79.64	54.39	82.89	39.09	72.00	84.01	54.43
Voltron-B	100	16.00	72.00	76.00	100.00	64.00	100.00	96.00	74.31	42.05	68.88	36.94	70.91	86.28	65.11
	200	32.00	72.00	76.00	100.00	60.00	96.00	88.00	71.57	38.17	67.53	31.01	70.17	86.61	62.39
	300	20.00	68.00	72.00	100.00	52.00	96.00	84.00	71.25	36.50	66.14	30.11	69.88	86.16	59.02
MAE-B	100	24.00	88.00	88.00	100.00	84.00	96.00	96.00	88.28	42.55	95.18	44.08	69.26	85.63	55.68
	200	28.00	76.00	84.00	100.00	84.00	88.00	88.00	77.13	38.49	88.22	32.75	69.02	85.14	56.81
	300	28.00	72.00	76.00	100.00	80.00	88.00	80.00	75.60	36.93	78.35	31.03	69.01	84.11	57.30
DINOv2-B	100	8.00	60.00	40.00	100.00	44.00	96.00	20.00	45.95	16.61	63.57	13.38	60.11	74.07	36.29
	200	8.00	68.00	40.00	100.00	64.00	88.00	16.00	37.96	15.81	51.44	12.59	59.56	74.18	32.14
	300	12.00	64.00	48.00	100.00	64.00	88.00	4.00	32.43	14.31	36.01	11.67	56.54	73.77	36.53
VC-1-B	100	20.00	76.00	76.00	100.00	76.00	100.00	76.00	72.35	43.14	92.77	27.31	68.67	84.19	62.00
	200	32.00	80.00	68.00	100.00	76.00	100.00	92.00	81.83	44.05	83.62	27.80	70.98	83.88	59.63
	300	24.00	68.00	80.00	100.00	80.00	88.00	88.00	83.01	41.25	77.60	28.53	70.89	84.76	59.51
RADIO	100	28.00	76.00	48.00	100.00	72.00	100.00	84.00	87.84	62.72	96.53	15.71	67.88	85.70	57.52
	200	36.00	76.00	44.00	100.00	72.00	96.00	52.00	80.26	57.39	95.93	15.26	67.51	85.67	57.81
	300	44.00	72.00	32.00	100.00	40.00	92.00	48.00	79.62	53.51	89.16	14.80	66.57	85.64	58.14
E-RADIO	100	32.00	84.00	64.00	100.00	84.00	96.00	96.00	71.47	53.41	93.01	50.19	70.75	87.17	46.97
	200	32.00	84.00	60.00	100.00	68.00	88.00	96.00	68.80	44.56	88.54	33.19	70.46	87.39	50.72
	300	28.00	80.00	60.00	100.00	72.00	88.00	80.00	65.96	33.56	98.14	32.64	69.18	87.09	51.31
SPA-B	100	20.00	84.00	84.00	100.00	88.00	100.00	100.00	80.50	45.08	91.38	48.90	71.16	86.04	59.03
	200	28.00	80.00	68.00	100.00	84.00	100.00	84.00	79.71	46.65	85.75	40.84	71.01	86.16	60.05
	300	24.00	80.00	88.00	100.00	92.00	100.00	92.00	74.70	48.97	81.60	34.92	71.16	85.16	61.94

1350
1351
1352
1353
1354
1355
1356
1357
1358
1359
1360
1361
1362
1363
1364
1365
1366
1367
1368
1369
1370
1371
1372
1373
1374
1375
1376
1377
1378
1379
1380
1381
1382
1383
1384
1385
1386
1387
1388
1389
1390
1391
1392
1393
1394
1395
1396
1397
1398
1399
1400
1401
1402
1403

Table 13: All results on Franka Kitchen.

Task	View	Seed	MoCoV3	MAE	DINOv2	CLIP	EVA	InternViT-300M	MVP	VC-1	SPA
Task 1	Left	100	86.00	76.00	84.00	72.00	78.00	74.00	66.00	74.00	84.00
		200	78.00	78.00	74.00	72.00	76.00	72.00	58.00	74.00	92.00
		300	80.00	80.00	78.00	62.00	82.00	70.00	64.00	74.00	80.00
	Right	100	82.00	80.00	86.00	78.00	78.00	72.00	82.00	78.00	86.00
		200	88.00	62.00	90.00	70.00	86.00	86.00	86.00	84.00	72.00
		300	86.00	82.00	92.00	82.00	86.00	76.00	92.00	78.00	86.00
Task 2	Left	100	60.00	56.00	48.00	26.00	40.00	22.00	40.00	32.00	48.00
		200	64.00	60.00	46.00	44.00	40.00	32.00	32.00	42.00	60.00
		300	58.00	54.00	40.00	26.00	32.00	34.00	30.00	50.00	66.00
	Right	100	62.00	54.00	56.00	26.00	44.00	26.00	32.00	54.00	48.00
		200	64.00	54.00	60.00	36.00	40.00	24.00	28.00	56.00	42.00
		300	64.00	52.00	50.00	38.00	40.00	30.00	34.00	44.00	42.00
Task 3	Left	100	16.00	24.00	18.00	18.00	22.00	24.00	6.00	24.00	28.00
		200	28.00	20.00	14.00	18.00	20.00	16.00	6.00	30.00	38.00
		300	22.00	16.00	14.00	10.00	26.00	22.00	8.00	26.00	30.00
	Right	100	46.00	26.00	38.00	22.00	14.00	8.00	32.00	12.00	10.00
		200	48.00	22.00	38.00	24.00	18.00	4.00	32.00	12.00	12.00
		300	54.00	34.00	52.00	14.00	12.00	6.00	26.00	14.00	16.00
Task 4	Left	100	32.00	36.00	26.00	22.00	34.00	12.00	16.00	36.00	22.00
		200	30.00	30.00	32.00	14.00	20.00	8.00	14.00	24.00	10.00
		300	24.00	46.00	28.00	14.00	32.00	4.00	20.00	36.00	16.00
	Right	100	38.00	24.00	28.00	22.00	32.00	12.00	26.00	12.00	30.00
		200	42.00	24.00	24.00	24.00	24.00	12.00	30.00	8.00	38.00
		300	46.00	16.00	32.00	28.00	36.00	16.00	26.00	12.00	30.00
Task 5	Left	100	36.00	18.00	8.00	16.00	24.00	22.00	26.00	28.00	20.00
		200	30.00	24.00	8.00	10.00	24.00	16.00	20.00	22.00	16.00
		300	22.00	22.00	10.00	12.00	16.00	14.00	28.00	30.00	18.00
	Right	100	24.00	46.00	20.00	4.00	14.00	10.00	26.00	22.00	30.00
		200	24.00	30.00	16.00	8.00	18.00	18.00	22.00	22.00	26.00
		300	14.00	36.00	16.00	12.00	10.00	12.00	20.00	16.00	22.00

Table 14: All results on Meta-World.

Method	MoCoV3	MAE	DINOv2	CLIP	EVA	InternViT-300M	MVP	VC-1	SPA
Seed	100 200 300	100 200 300	100 200 300	100 200 300	100 200 300	100 200 300	100 200 300	100 200 300	100 200 300
ButtonPressWall	100 100 100	100 100 100	95 90 95	100 100 100	95 95 100	95 100 95	100 100 100	100 100 100	100 100 100
DoorClose	100 100 100	100 100 100	100 100 100	100 100 100	100 100 100	100 100 100	100 100 100	100 100 100	100 100 100
DoorUnlock	70 65 80	70 65 85	35 35 30	60 50 60	85 85 90	80 65 75	75 70 85	80 75 90	80 75 80
DrawerClose	100 100 100	100 100 100	100 100 100	100 100 100	100 100 100	100 100 100	100 100 100	100 100 100	100 100 100
DrawerOpen	80 70 85	85 65 75	60 40 60	90 80 80	60 55 75	70 75 75	95 75 85	85 85 80	90 60 75
FaucetClose	70 80 55	60 80 60	55 65 35	70 80 50	65 75 60	50 65 50	70 75 60	65 75 100	70 80 65
PlateSlide	90 95 100	95 100 100	65 70 80	85 95 80	100 100 100	85 95 90	100 100 100	100 95 100	95 95 95
PlateSlideBack	80 65 85	85 65 85	90 75 90	85 75 90	80 65 90	85 80 90	85 70 90	80 70 90	80 70 85
PlateSlideSide	85 90 95	95 90 95	90 85 85	80 85 95	100 95 100	90 95 90	80 90 95	100 95 90	90 90 95
WindowClose	100 100 100	100 100 100	70 90 100	100 100 95	95 100 100	100 100 100	100 100 100	100 100 100	100 100 100
Basketball	85 95 95	95 100 100	70 55 65	85 85 70	95 85 80	90 80 95	95 100 95	90 100 95	95 100 100
BinPicking	30 45 40	20 10 35	10 15 10	30 30 25	20 5 45	10 10 10	25 20 15	30 30 30	40 25 30
BoxClose	80 80 80	75 80 70	35 45 30	80 70 60	55 70 55	60 65 40	80 80 65	80 95 60	80 80 65
CoffeePush	45 50 40	40 55 30	30 25 15	45 40 55	45 35 40	45 30 25	25 45 25	30 45 55	35 40 30
Assembly	70 60 55	55 65 45	30 35 25	45 55 50	45 50 40	30 25 30	60 60 45	60 60 50	50 55 50
Disassemble	40 55 50	30 45 45	30 20 45	55 50 60	30 50 50	40 45 50	40 45 45	40 30 35	40 45 55
PushWall	25 35 30	20 30 40	40 30 45	35 30 35	25 35 30	15 15 25	30 35 35	55 55 60	30 40 45
ShelfPlace	35 35 20	25 45 20	30 30 35	30 35 30	25 20 15	15 15 15	25 25 15	25 15 15	15 35 15
DoorOpen	95 90 90	100 95 95	95 80 95	85 75 90	80 90 100	50 55 60	80 75 95	95 95 95	85 100 95
ButtonPress	75 85 85	85 100 100	80 95 85	55 70 75	80 90 90	85 90 80	85 90 95	80 90 85	100 95 100
SweepInto	45 45 40	55 55 45	50 50 40	45 45 40	45 25 30	35 25 30	45 50 40	55 50 50	50 50 45
DoorLock	100 85 85	90 100 100	95 90 85	85 85 75	95 100 95	80 90 95	85 100 95	100 100 90	80 95 85
ReachWall	70 70 80	75 85 70	85 80 85	90 90 80	65 75 85	60 55 55	75 65 75	75 80 80	75 80 70
Hammer	25 45 30	30 30 30	40 45 35	25 35 25	30 35 20	20 20 20	30 35 30	45 40 55	30 40 30
StickPush	95 95 100	80 90 95	90 90 90	75 85 85	90 85 100	60 80 85	90 95 90	85 85 95	90 90 85
ButtonPressTopdown	80 80 75	80 85 80	80 90 90	80 90 70	55 65 55	45 55 55	80 85 80	75 80 70	80 85 80
HandlePressSide	100 100 100	100 100 100	95 100 90	80 100 90	100 100 95	85 100 90	95 100 100	75 100 80	90 100 100
PlateSlideBackSide	100 100 100	100 95 95	100 100 100	100 100 100	100 100 100	100 100 100	100 100 100	100 100 100	100 100 100
Sweep	50 80 70	35 60 60	65 85 95	60 85 75	35 50 55	15 60 35	35 70 65	35 65 65	30 65 55
ButtonPressTopdownWall	45 70 80	45 75 75	70 75 75	45 60 70	30 45 65	20 55 45	30 60 70	50 85 80	45 65 75
HandlePress	85 95 95	80 100 75	75 100 80	90 100 90	85 100 85	65 90 75	80 95 75	85 100 90	85 100 80
Push	25 30 30	25 30 30	30 25 40	25 15 30	30 25 20	25 20 20	25 20 25	40 30 25	30 15 35
CoffeePull	55 55 55	40 45 40	20 30 20	50 70 40	40 45 45	40 40 25	55 55 40	55 55 60	55 55 55
DialTurn	80 65 80	85 75 75	40 30 35	80 95 90	65 65 80	70 70 55	70 65 75	80 95 75	85 85 75
Reach	90 75 80	90 75 80	70 75 85	95 95 100	85 80 75	95 80 90	80 70 75	70 80 80	85 70 85
CoffeeButton	85 95 75	100 100 95	85 80 60	95 100 85	90 100 95	90 85 85	100 100 90	90 100 80	100 100 100
PickPlaceWall	45 35 65	40 25 45	15 10 20	35 40 50	20 25 35	30 25 25	25 35 40	35 20 45	40 35 55
StickPull	35 35 25	15 40 20	25 10 5	45 40 45	25 35 15	25 25 15	15 30 25	30 30 30	25 35 30
HandInsert	35 30 30	30 25 25	20 20 20	45 45 40	20 25 20	25 30 25	40 40 35	40 30 40	40 50 40
PegInsertSide	40 35 40	50 35 45	25 15 10	45 30 20	45 25 30	30 20 25	45 45 30	50 25 35	55 45 60
PickPlace	35 30 30	25 45 15	15 10 10	25 15 30	25 30 25	30 10 30	20 35 25	25 20 20	25 30 40
FaucetOpen	95 95 100	100 100 100	80 80 100	100 95 100	95 95 100	80 85 95	100 100 100	100 100 100	95 100 100
PushBack	65 70 60	40 55 40	15 15 25	30 45 25	35 35 45	15 35 25	40 45 45	45 55 25	35 55 50
LeverPull	70 80 80	80 70 75	15 30 35	55 85 80	70 65 70	60 55 55	65 80 65	65 80 70	85 70 80
HandlePull	85 85 80	85 80 85	45 55 40	75 75 80	80 60 65	45 70 65	80 90 80	70 85 75	100 90 90
Soccer	25 40 35	50 30 25	15 10 15	45 40 30	35 35 25	20 20 30	30 30 35	20 20 20	25 50 25
WindowOpen	65 80 80	55 80 85	60 50 65	50 65 60	65 80 75	55 75 75	60 70 70	60 70 75	55 85 65
PickOutOfHole	65 75 80	65 65 60	60 55 60	70 70 50	60 55 50	60 55 55	65 55 60	70 75 60	65 60 75

1458

1459

Table 15: All results on RL Bench.

Method	MoCoV3	MAE	DINOv2	CLIP	EVA	InternViT 300M	MVP	VC-1	SPA
<i>Group 1</i>									
1462	100	100	100	100	100	100	100	100	100
1463	100	100	96	96	96	100	96	100	100
1464	100	100	100	100	100	100	100	100	100
1465	80	76	76	68	80	72	68	76	80
1466	0	84	96	24	4	0	100	100	4
1467	100	96	88	100	96	100	96	100	100
1468	88	88	92	88	84	84	88	88	96
1469	64	60	28	64	60	44	52	60	68
1470	8	4	0	4	8	8	12	4	4
1471	0	0	0	0	0	0	0	0	0
1472	60	72	72	68	56	60	84	68	68
1473	60	96	88	100	96	80	92	96	92
1474	100	100	100	100	100	100	100	100	100
1475	88	68	84	88	52	80	28	88	64
1476	100	100	100	100	100	100	96	96	100
1477	96	96	96	96	84	80	80	96	100
1478	12	12	20	4	16	4	0	12	16
1479	88	96	92	100	88	88	92	96	96
1480	92	92	88	96	96	88	96	96	96
1481	88	84	84	96	88	92	96	100	100
1482	100	100	100	100	100	100	100	88	100
1483	96	96	96	100	96	100	96	96	96
1484	28	84	80	44	88	40	64	92	84
1485	92	100	100	92	100	96	100	100	100
1486	12	20	20	24	24	20	16	8	68
1487	56	44	72	80	48	72	52	60	84
1488	96	96	96	96	96	96	100	100	100
1489	64	68	48	68	64	72	64	60	68
1490	100	100	100	100	100	100	100	100	100
1491	80	92	92	88	92	96	88	92	100
1492	96	96	96	96	96	96	100	100	96
1493	96	96	96	96	96	96	100	100	96
1494	100	100	100	100	100	100	96	100	100
1495	44	32	48	36	48	40	40	44	44
1496	92	92	88	72	76	84	76	88	92
1497	100	96	100	100	100	100	100	100	100
<i>Group 2</i>									
1498	0	8	4	0	0	4	0	0	4
1499	4	8	0	4	4	8	4	4	8
1500	12	4	4	0	0	0	0	12	4
1501	12	16	40	4	12	0	28	8	28
1502	0	0	0	0	0	0	0	0	0
1503	0	0	0	0	0	0	0	0	0
1504	92	96	96	96	92	100	100	88	96
1505	96	100	96	92	84	96	88	92	96
1506	52	36	36	36	36	52	32	32	48
1507	20	28	24	36	40	12	32	36	36
1508	0	0	0	0	0	4	0	0	4
1509	100	96	96	100	96	96	100	100	100
1510	88	96	92	96	92	80	96	96	96
1511	100	100	100	100	100	100	100	100	100
1512	100	100	100	100	100	100	100	100	100
1513	92	92	96	96	100	96	100	96	100
1514	100	100	100	100	100	96	100	100	100
1515	80	88	100	88	88	80	88	92	96
1516	12	24	24	28	28	20	20	28	16
1517	88	92	96	88	92	84	88	88	100
1518	40	56	52	52	48	56	64	68	64
1519	72	76	68	72	80	88	80	76	80
1520	20	36	32	28	36	20	44	36	56
1521	100	92	76	96	92	88	84	92	96
1522	8	0	12	12	0	4	12	8	12
1523	76	80	68	68	88	92	92	80	80
1524	96	96	100	100	96	100	96	100	100
1525	80	100	88	92	92	88	96	88	88
1526	100	100	88	96	100	80	96	100	100
1527	96	100	88	92	100	96	100	100	100
1528	100	96	96	96	96	96	84	96	96
1529	32	68	56	60	80	20	24	20	60
1530	44	52	48	44	36	64	52	32	64
1531	8	4	12	8	4	20	4	4	16
1532	32	36	32	24	44	36	24	32	60

Table 16: All results on LIBERO-OBJECT, LIBERO-SPATIAL, LIBERO-GOAL, LIBERO-10.

	MoCoV3	MAE	DINOv2	CLIP	EVA	InternViT-300M	InternViT-6B	MVP	VC-1	SPA
Seed	100 200 300	100 200 300	100 200 300	100 200 300	100 200 300	100 200 300	100 200 300	100 200 300	100 200 300	100 200 300
<i>LIBERO-OBJECT</i>										
0	0.65 0.60 0.65	0.65 0.45 0.55	0.65 0.80 0.85	0.80 0.75 0.65	1.00 0.70 0.95	0.80 0.65 0.60	0.70 0.85 0.50	0.80 0.90 0.65	0.80 0.50 0.60	0.90 0.95 0.95
1	0.35 0.35 0.55	0.90 0.75 0.80	0.30 0.50 0.75	0.40 0.30 0.05	0.65 0.30 0.70	0.15 0.40 0.20	0.60 0.25 0.45	0.05 0.80 0.60	0.40 0.65 0.45	0.65 0.70 0.45
2	0.90 0.85 0.95	0.90 0.40 0.95	0.85 0.50 0.90	0.70 0.80 0.75	0.85 0.75 0.75	0.90 0.85 0.80	0.85 0.45 0.85	0.80 0.85 0.90	1.00 0.95 0.95	0.90 0.95 0.80
3	0.55 0.70 0.65	0.90 0.15 0.90	0.30 0.65 0.90	0.25 0.45 0.60	0.80 0.80 0.90	0.75 0.70 0.40	1.00 0.50 0.55	0.70 0.65 0.85	0.95 0.75 0.60	0.70 0.90 0.90
4	0.65 0.85 0.85	0.80 0.90 0.75	0.75 0.55 0.75	0.35 0.75 0.65	0.95 0.75 1.00	0.90 1.00 0.85	0.90 0.70 0.80	0.80 0.75 0.70	0.90 0.85 0.90	0.90 1.00 0.95
5	0.50 0.70 0.80	0.70 0.35 0.60	0.55 0.75 0.60	0.25 0.70 0.45	0.75 0.75 0.65	0.85 0.60 0.75	0.60 0.35 0.50	0.55 0.40 0.80	0.65 0.70 0.70	0.25 0.15 0.65
6	0.35 0.50 0.65	0.60 0.65 0.65	0.55 0.70 0.70	0.35 0.55 0.60	0.40 0.35 0.25	0.65 0.60 0.55	0.30 0.10 0.35	0.25 0.50 0.65	0.50 0.50 0.30	0.50 0.70 0.80
7	0.75 0.75 0.80	0.90 0.40 0.75	0.55 0.30 0.70	0.40 0.35 0.40	0.55 0.75 0.70	0.80 0.40 0.60	0.60 0.65 0.70	0.60 0.45 0.65	0.80 0.75 0.50	0.80 0.75 0.65
8	0.50 0.95 0.90	1.00 0.95 1.00	0.50 0.35 0.50	0.45 0.45 0.35	1.00 0.75 0.85	0.70 0.65 0.75	0.50 0.40 0.75	0.65 0.55 0.70	0.80 0.90 0.50	0.85 0.95 0.90
9	0.45 0.50 0.40	0.60 0.65 0.95	0.80 0.90 0.95	0.50 0.70 0.30	0.85 0.75 0.75	0.85 0.95 0.65	0.90 0.60 0.15	0.65 0.60 0.30	0.70 0.70 0.65	0.60 0.95 0.90
<i>LIBERO-SPATIAL</i>										
0	0.35 0.55 0.45	0.45 0.40 0.70	0.65 0.50 0.60	0.25 0.20 0.35	0.70 0.75 0.65	0.55 0.65 0.55	0.55 0.50 0.30	0.75 0.75 0.60	0.35 0.55 0.60	0.45 0.50 0.35
1	0.65 0.70 0.70	0.80 0.80 0.50	0.55 0.30 0.35	0.75 0.75 0.70	0.55 0.70 0.25	0.35 0.50 0.50	1.00 1.00 0.90	0.60 0.40 0.60	0.45 0.65 0.80	0.65 0.65 0.85
2	0.55 0.50 0.50	0.35 0.60 0.40	0.20 0.05 0.55	0.10 0.00 0.40	0.70 0.80 0.50	0.70 0.75 0.60	0.75 0.60 0.20	0.85 0.55 0.75	0.45 0.45 0.70	0.50 0.50 0.40
3	0.50 0.70 0.75	0.55 0.60 0.75	0.80 0.70 0.95	0.15 0.40 0.30	0.85 0.90 0.85	0.35 0.50 0.40	0.40 0.30 0.15	0.95 0.55 0.60	0.50 0.70 0.65	0.55 0.85 0.60
4	0.15 0.15 0.20	0.55 0.70 0.80	0.50 0.05 0.45	0.35 0.30 0.20	0.45 0.55 0.40	0.35 0.25 0.40	0.25 0.15 0.15	0.60 0.50 0.70	0.60 0.60 0.80	0.70 0.70 0.50
5	0.45 0.10 0.10	0.65 0.40 0.30	0.30 0.20 0.35	0.55 0.45 0.45	0.65 0.50 0.45	0.40 0.30 0.70	0.55 0.60 0.60	0.55 0.30 0.25	0.05 0.05 0.15	0.35 0.35 0.30
6	0.30 0.35 0.45	0.55 0.25 0.95	0.40 0.30 0.40	0.20 0.25 0.10	0.75 0.70 0.85	0.45 0.55 0.55	0.40 0.35 0.05	0.45 0.75 0.65	0.60 0.70 0.35	0.35 0.45 0.30
7	0.10 0.20 0.25	0.50 0.35 0.45	0.05 0.00 0.10	0.30 0.15 0.25	0.30 0.30 0.20	0.30 0.60 0.65	0.15 0.05 0.05	0.60 0.65 0.60	0.10 0.20 0.40	0.40 0.15 0.45
8	0.55 0.70 0.50	0.35 0.65 0.70	0.40 0.15 0.55	0.30 0.55 0.30	0.85 0.70 0.60	0.30 0.55 0.60	0.65 0.40 0.35	0.70 0.40 0.55	0.70 0.60 0.70	0.75 0.70 0.40
9	0.55 0.05 0.10	0.85 0.75 0.50	0.20 0.05 0.25	0.20 0.20 0.20	0.55 0.50 0.30	0.35 0.50 0.30	0.45 0.40 0.35	0.45 0.45 0.30	0.50 0.55 0.65	0.35 0.50 0.45
<i>LIBERO-GOAL</i>										
0	0.45 0.70 0.75	0.70 0.85 0.80	0.15 0.10 0.30	0.25 0.40 0.35	0.70 0.60 0.60	0.75 0.65 0.75	0.25 0.35 0.35	0.75 0.60 0.95	0.45 0.85 1.00	0.85 1.00 0.85
1	0.70 0.60 0.80	0.65 0.50 0.90	0.25 0.55 0.25	0.20 0.15 0.25	0.70 0.80 0.80	0.90 0.90 1.00	0.40 0.15 0.15	0.90 0.80 0.95	0.65 0.65 0.65	1.00 0.85 0.90
2	0.50 0.20 0.15	0.10 0.40 0.35	0.10 0.05 0.15	0.30 0.25 0.30	0.65 0.75 0.75	0.40 0.75 0.45	0.50 0.35 0.35	0.45 0.25 0.65	0.40 0.60 0.35	0.50 0.55 0.35
3	0.75 0.45 0.60	0.40 0.75 0.55	0.20 0.10 0.10	0.05 0.20 0.55	0.30 0.15 0.15	0.30 0.50 0.65	0.20 0.25 0.25	0.70 0.70 0.15	0.75 0.55 0.50	0.65 0.35 0.80
4	0.20 0.25 0.05	0.35 0.40 0.25	0.10 0.00 0.05	0.40 0.30 0.15	0.15 0.10 0.10	0.20 0.15 0.10	0.15 0.20 0.20	0.55 0.60 0.25	0.15 0.30 0.30	0.30 0.35 0.35
5	0.10 0.75 0.80	0.60 0.85 0.80	0.65 0.50 0.50	0.35 0.45 0.50	0.80 0.75 0.75	0.70 0.55 0.45	0.55 0.45 0.45	0.80 0.75 0.85	0.65 0.75 0.80	0.80 0.65 0.65
6	0.45 0.05 0.15	0.00 0.10 0.05	0.00 0.05 0.00	0.10 0.10 0.00	0.00 0.65 0.65	0.50 0.40 0.30	0.00 0.00 0.00	0.15 0.35 0.70	0.25 0.50 0.45	0.40 0.30 0.35
7	0.25 0.75 0.90	0.80 0.65 1.00	0.45 0.45 0.35	0.50 0.65 0.80	1.00 1.00 1.00	1.00 1.00 0.95	0.70 0.85 0.85	0.95 1.00 0.95	1.00 0.95 0.70	0.95 1.00 1.00
8	0.50 0.80 0.75	0.85 0.55 0.90	0.45 0.40 0.20	0.60 0.25 0.50	0.90 0.35 0.35	0.95 0.65 0.55	0.65 0.25 0.25	0.70 0.65 0.70	0.50 0.75 0.55	0.80 0.65 0.80
9	0.10 0.65 0.60	0.50 0.20 0.50	0.10 0.00 0.10	0.10 0.10 0.00	0.15 0.70 0.70	0.60 0.40 0.20	0.15 0.35 0.35	0.30 0.50 0.55	0.20 0.35 0.70	0.55 0.60 0.45
<i>LIBERO-10</i>										
0	0.15 0.20 0.10	0.15 0.25 0.10	0.00 0.05 0.10	0.00 0.05 0.05	0.25 0.35 0.10	0.35 0.10 0.25	0.15 0.15 0.00	0.05 0.15 0.20	0.10 0.45 0.25	0.05 0.10 0.05
1	0.25 0.20 0.20	0.30 0.15 0.25	0.15 0.15 0.15	0.40 0.30 0.15	0.65 0.10 0.60	0.15 0.50 0.45	0.00 0.25 0.35	0.15 0.10 0.15	0.20 0.40 0.15	0.25 0.05 0.45
2	0.70 0.60 0.75	0.30 0.60 0.75	0.55 0.45 0.50	0.25 0.45 0.40	0.75 0.55 0.65	0.45 0.80 0.55	0.70 0.80 0.75	0.75 0.65 0.55	0.85 1.00 0.90	0.70 0.80 0.50
3	0.50 0.80 0.55	0.55 0.60 0.80	0.40 0.45 0.45	0.60 0.65 0.60	0.80 0.90 0.75	0.75 0.65 0.50	0.75 0.60 0.60	0.75 0.70 0.65	0.80 0.70 0.70	0.70 0.90 0.70
4	0.25 0.20 0.05	0.35 0.25 0.30	0.10 0.10 0.05	0.20 0.05 0.05	0.15 0.10 0.15	0.15 0.15 0.05	0.15 0.20 0.15	0.25 0.20 0.35	0.30 0.25 0.30	0.40 0.30 0.25
5	0.40 0.60 0.75	0.55 0.70 0.80	0.50 0.65 0.75	0.40 0.40 0.30	0.85 0.65 0.75	0.75 0.55 0.75	0.45 0.55 0.45	0.60 0.70 0.75	0.80 0.90 0.60	0.70 0.70 0.45
6	0.20 0.25 0.10	0.40 0.35 0.40	0.05 0.20 0.05	0.25 0.15 0.15	0.20 0.30 0.35	0.10 0.15 0.20	0.20 0.25 0.05	0.40 0.30 0.35	0.30 0.10 0.20	0.20 0.20 0.15
7	0.40 0.30 0.25	0.50 0.50 0.50	0.10 0.30 0.60	0.30 0.40 0.20	0.45 0.30 0.25	0.40 0.35 0.35	0.35 0.70 0.25	0.35 0.30 0.25	0.30 0.25 0.30	0.50 0.45 0.40
8	0.10 0.10 0.15	0.10 0.30 0.20	0.35 0.20 0.05	0.10 0.10 0.10	0.15 0.20 0.10	0.20 0.00 0.25	0.05 0.20 0.05	0.10 0.30 0.20	0.25 0.30 0.25	0.25 0.05 0.15
9	0.20 0.60 0.35	0.40 0.65 0.30	0.35 0.25 0.45	0.45 0.45 0.30	0.40 0.70 0.50	0.50 0.45 0.60	0.50 0.25 0.40	0.40 0.55 0.50	0.00 0.00 0.00	0.50 0.65 0.50

Table 17: All results on LIBERO-90.

Seed	MoCoV3			MAE			DINOv2			CLIP			EVA			InternViT-300M			InternViT-6B			MVP			VC-1			SPA		
	100	200	300	100	200	300	100	200	300	100	200	300	100	200	300	100	200	300	100	200	300	100	200	300	100	200	300	100	200	300
LIBERO-90																														
0	0.95	0.85	0.90	1.00	0.90	0.80	0.80	1.00	0.60	0.90	0.80	0.80	1.00	1.00	1.00	0.90	0.80	0.85	0.75	0.80	0.95	0.95	0.95	1.00	0.95	1.00	0.95	1.00	1.00	0.95
1	0.60	0.35	0.60	0.35	0.50	0.15	0.50	0.55	0.30	0.40	0.65	0.35	0.70	0.50	0.25	0.30	0.45	0.40	0.25	0.35	0.55	0.80	0.55	0.30	0.40	0.50	0.05	0.65	0.40	0.50
2	0.85	0.50	0.80	0.55	0.55	0.20	0.65	0.60	0.30	0.45	0.30	0.50	0.35	0.50	0.70	0.85	0.65	0.80	0.25	0.35	0.30	0.45	0.70	0.70	0.75	0.55	0.35	0.70	0.85	0.60
3	0.10	0.10	0.00	0.05	0.00	0.00	0.05	0.00	0.00	0.15	0.00	0.00	0.00	0.10	0.15	0.00	0.05	0.05	0.00	0.00	0.05	0.10	0.00	0.05	0.05	0.10	0.00	0.10	0.10	0.00
4	0.40	0.05	0.20	0.30	0.25	0.30	0.15	0.40	0.55	0.40	0.40	0.35	0.10	0.25	0.15	0.40	0.05	0.25	0.20	0.45	0.40	0.30	0.40	0.15	0.25	0.05	0.15	0.15	0.15	0.30
5	0.05	0.05	0.05	0.10	0.05	0.20	0.00	0.20	0.00	0.05	0.05	0.20	0.25	0.25	0.10	0.10	0.05	0.30	0.20	0.10	0.25	0.05	0.15	0.10	0.10	0.05	0.05	0.35	0.00	0.15
6	0.10	0.00	0.00	0.00	0.00	0.05	0.05	0.05	0.10	0.05	0.10	0.00	0.00	0.00	0.05	0.00	0.00	0.00	0.05	0.10	0.10	0.00	0.05	0.00	0.00	0.00	0.00	0.00	0.05	0.05
7	0.35	0.30	0.65	0.20	0.60	0.30	0.35	0.25	0.40	0.50	0.60	0.35	0.60	0.10	0.20	0.15	0.25	0.10	0.40	0.25	0.45	0.50	0.20	0.40	0.20	0.30	0.25	0.30	0.30	0.65
8	0.10	0.15	0.00	0.05	0.20	0.10	0.15	0.25	0.10	0.20	0.10	0.10	0.10	0.05	0.00	0.05	0.00	0.10	0.20	0.15	0.20	0.10	0.00	0.20	0.10	0.05	0.20	0.10	0.15	0.15
9	0.30	0.25	0.35	0.50	0.25	0.30	0.35	0.60	0.70	0.25	0.20	0.50	0.25	0.10	0.50	0.10	0.10	0.25	0.60	0.25	0.30	0.25	0.15	0.45	0.25	0.05	0.35	0.25	0.20	0.25
10	0.50	0.75	0.50	0.50	0.60	0.55	0.65	0.60	0.60	0.90	0.45	0.55	0.40	0.85	0.35	0.35	0.05	0.25	0.45	0.45	0.65	0.40	0.50	0.55	0.45	0.75	0.40	0.40	0.35	0.35
11	0.45	0.35	0.75	0.45	0.70	0.65	0.35	0.20	0.15	0.40	0.70	0.55	0.80	0.25	0.70	0.50	0.50	0.10	0.35	0.25	0.45	0.80	0.60	0.95	0.70	0.75	0.60	0.60	0.60	0.65
12	0.15	0.15	0.10	0.15	0.15	0.05	0.20	0.20	0.15	0.10	0.05	0.05	0.10	0.25	0.05	0.05	0.00	0.00	0.25	0.30	0.10	0.15	0.10	0.10	0.20	0.25	0.10	0.05	0.10	0.15
13	0.20	0.35	0.30	0.15	0.30	0.20	0.30	0.35	0.10	0.30	0.40	0.35	0.30	0.10	0.45	0.20	0.35	0.40	0.25	0.15	0.55	0.30	0.30	0.15	0.45	0.10	0.10	0.10	0.20	0.10
14	0.05	0.10	0.00	0.30	0.30	0.20	0.10	0.10	0.15	0.15	0.40	0.20	0.25	0.35	0.10	0.15	0.15	0.05	0.20	0.15	0.10	0.20	0.35	0.10	0.20	0.10	0.20	0.15	0.15	0.10
15	0.60	0.75	0.45	0.70	0.50	0.65	0.35	0.50	0.55	0.45	0.65	0.40	0.70	0.75	0.40	0.40	0.65	0.50	0.35	0.55	0.45	0.70	0.60	0.55	0.80	0.80	0.70	0.65	0.80	0.55
16	0.05	0.20	0.00	0.30	0.15	0.05	0.10	0.10	0.05	0.10	0.00	0.10	0.20	0.20	0.15	0.15	0.15	0.20	0.05	0.00	0.10	0.15	0.05	0.10	0.00	0.15	0.15	0.15	0.10	0.15
17	0.05	0.15	0.15	0.10	0.25	0.05	0.05	0.10	0.05	0.05	0.00	0.05	0.05	0.20	0.15	0.10	0.10	0.15	0.00	0.10	0.00	0.20	0.10	0.20	0.15	0.10	0.10	0.05	0.10	0.10
18	0.45	0.40	0.60	0.40	0.75	0.65	0.30	0.35	0.40	0.45	0.25	0.35	0.25	0.35	0.60	0.40	0.05	0.70	0.60	0.50	0.35	0.35	0.25	0.45	0.30	0.60	0.35	0.60	0.35	0.55
19	0.30	0.30	0.25	0.35	0.40	0.20	0.20	0.05	0.35	0.45	0.45	0.30	0.30	0.35	0.25	0.15	0.25	0.20	0.35	0.30	0.15	0.55	0.30	0.40	0.40	0.45	0.35	0.60	0.30	0.55
20	0.85	0.75	0.80	1.00	1.00	0.95	0.95	1.00	1.00	0.75	0.85	0.30	1.00	1.00	1.00	0.95	0.95	0.90	1.00	0.50	0.80	0.90	1.00	1.00	1.00	1.00	1.00	1.00	1.00	1.00
21	0.40	0.20	0.40	0.35	0.25	0.30	0.25	0.40	0.20	0.25	0.10	0.45	0.30	0.70	0.05	0.00	0.05	0.10	0.35	0.10	0.30	0.40	0.15	0.30	0.30	0.70	0.60	0.65	0.40	0.60
22	0.90	0.95	0.95	1.00	0.85	0.95	0.25	0.60	0.40	0.75	0.75	0.75	0.95	1.00	0.95	0.85	0.95	0.60	0.45	0.25	0.25	0.90	1.00	1.00	0.90	0.90	0.95	1.00	0.95	1.00
23	0.15	0.05	0.15	0.05	0.10	0.00	0.05	0.10	0.05	0.00	0.00	0.05	0.00	0.00	0.00	0.00	0.00	0.00	0.20	0.25	0.05	0.00	0.00	0.00	0.00	0.00	0.00	0.00	0.00	0.00
24	0.80	0.30	0.85	0.85	0.50	0.80	0.60	0.50	0.65	0.70	0.45	0.60	0.70	0.70	0.80	0.40	0.65	0.60	0.55	0.80	0.45	0.65	0.60	0.90	0.90	0.80	0.80	0.90	0.80	0.75
25	1.00	0.80	0.85	1.00	1.00	0.90	0.75	0.90	0.90	0.80	0.95	0.90	0.90	1.00	0.95	0.70	0.70	0.85	0.95	0.60	0.65	1.00	0.85	1.00	1.00	1.00	1.00	1.00	1.00	1.00
26	0.15	0.20	0.25	0.25	0.40	0.40	0.05	0.30	0.40	0.45	0.05	0.15	0.05	0.30	0.15	0.25	0.40	0.20	0.25	0.15	0.20	0.20	0.30	0.60	0.25	0.45	0.25	0.25	0.20	0.20
27	0.30	0.15	0.20	0.35	0.35	0.10	0.05	0.10	0.00	0.35	0.05	0.10	0.05	0.20	0.05	0.05	0.15	0.00	0.10	0.10	0.05	0.35	0.20	0.30	0.10	0.45	0.40	0.10	0.40	0.20
28	0.90	0.90	1.00	0.95	0.70	0.70	0.80	0.50	0.80	0.90	0.75	0.90	0.95	1.00	0.85	0.90	0.85	1.00	0.50	0.60	0.45	0.85	0.75	0.90	0.75	0.95	0.60	0.90	0.65	0.90
29	0.15	0.50	0.35	0.60	0.55	0.20	0.50	0.50	0.40	0.50	0.50	0.40	0.65	0.30	0.30	0.15	0.30	0.40	0.25	0.35	0.25	0.35	0.50	0.25	0.60	0.60	0.10	0.30	0.35	0.70
30	0.15	0.25	0.15	0.60	0.35	0.35	0.35	0.10	0.50	0.25	0.20	0.45	0.30	0.70	0.20	0.10	0.15	0.20	0.50	0.20	0.25	0.00	0.05	0.20	0.10	0.25	0.10	0.40	0.25	0.40
31	0.70	0.60	0.80	0.70	0.75	0.60	0.45	0.70	0.75	0.95	0.65	0.95	0.80	0.75	0.45	0.50	0.55	0.35	0.95	0.80	0.85	0.80	0.70	0.75	0.75	0.75	0.45	0.70	0.90	0.80
32	0.30	0.05	0.20	0.05	0.10	0.05	0.00	0.00	0.05	0.35	0.10	0.10	0.20	0.10	0.15	0.10	0.15	0.10	0.05	0.15	0.05	0.20	0.25	0.10	0.15	0.10	0.05	0.20	0.10	0.05
33	0.50	0.55	0.40	0.15	0.30	0.30	0.10	0.20	0.35	0.30	0.25	0.30	0.00	0.50	0.40	0.35	0.20	0.25	0.25	0.25	0.30	0.20	0.35	0.40	0.35	0.45	0.65	0.15	0.15	0.15
34	0.30	0.35	0.30	0.40	0.40	0.25	0.35	0.40	0.15	0.40	0.40	0.50	0.10	0.40	0.10	0.15	0.05	0.25	0.35	0.30	0.50	0.25	0.30	0.30	0.55	0.25	0.05	0.30	0.10	0.10
35	0.65	0.40	0.60	0.85	0.95	0.75	0.80	0.80	0.60	0.65	0.55	0.90	0.90	1.00	0.80	0.10	0.20	0.55	0.85	0.75	0.70	0.85	0.80	0.85	0.25	0.80	0.55	1.00	0.70	1.00
36	0.05	0.10	0.15	0.05	0.00	0.00	0.00	0.25	0.05	0.05	0.05	0.00	0.15	0.20	0.10	0.15	0.10	0.25	0.00	0.00	0.10	0.20	0.00	0.15	0.30	0.05	0.20	0.05	0.20	0.10
37	0.35	0.30	0.40	0.55	0.20	0.25	0.65	0.50	0.35	0.30	0.60	0.60	0.70	0.80	0.60	0.45	0.55	0.45	0.50	0.55	0.55	0.45	0.45	0.50	0.45	0.75	0.35	0.75	0.50	0.55
38	0.50	0.30	0.45	0.55	0.50	0.35	0.25	0.15	0.30	0.50	0.45	0.30	0.50	0.20	0.35	0.35	0.55	0.45	0.35	0.50	0.35	0.70	0.40	0.55	0.70	0.65	0.30	0.70	0.45	0.45
39	0.80	0.80	0.75	0.45	0.70	0.60	0.60	0.55	0.65	0.60	0.65	0.70	0.65	0.85	0.55	0.60	0.15	0.60	0.65	0.60	0.60	0.45	0.40	0.70	0.30	0.70	0.60	0.60	0.45	0.65
40	0.40	0.50	0.20	0.40	0.30	0.40	0.30	0.45	0.55	0.50	0.25	0.30	0.70	0.65	0.30	0.25	0.60	0.25	0.55	0.40	0.25	0.65	0.70	0.80	0.35	0.45	0.25	0.55	0.35	0.30
41	0.20	0.60	0.40	0.50	0.45	0.60	0.35	0.25	0.55	0.20	0.45	0.50	0.85	0.45	0.50	0.45	0.65	0.45	0.20	0.30	0.35	0.55	0.80	0.20	0.35	0.50	0.65	0.65	0.80	0.40

1620
1621
1622
1623
1624
1625
1626
1627
1628
1629
1630
1631
1632
1633
1634
1635
1636
1637
1638
1639
1640
1641
1642
1643
1644
1645
1646
1647
1648
1649
1650
1651
1652
1653
1654
1655
1656
1657
1658
1659
1660
1661
1662
1663
1664
1665
1666
1667
1668
1669
1670
1671
1672
1673

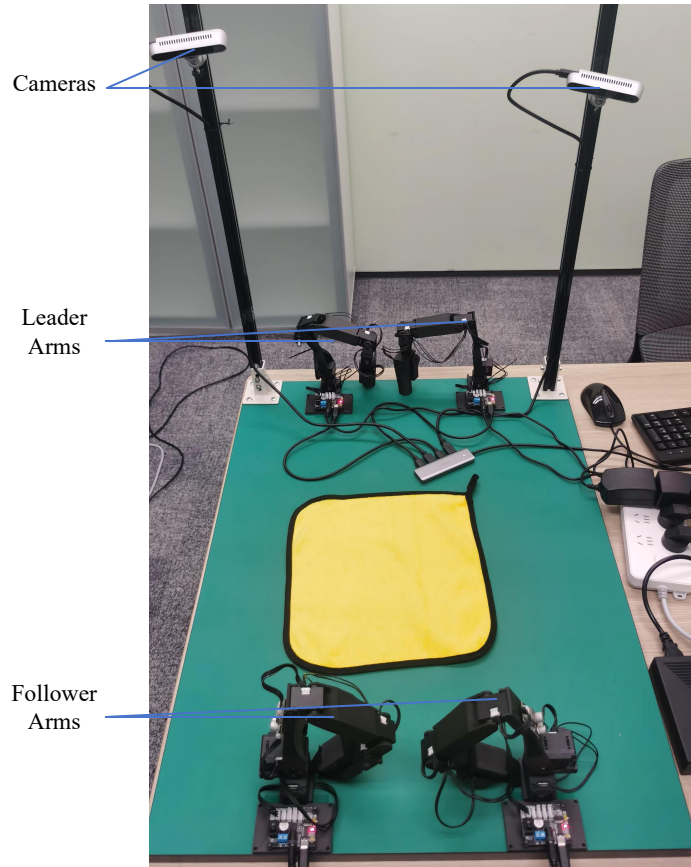


Figure 8: Real-world hardware platform.